Investigation into how the reduction of length scales affects the flow of viscoelastic fluid in parellel plate geometries

Martyn Taylor

August 22, 2005

Abstract

The question of whether minaturisation of flow geometries for viscoelastic fluids effects the flow patterns is explored. The problem is formulated and solved numerically using finite element methods for both a standard length scale and a micron length scale, with subsequent lengths in between investigated where necessary in order to draw conclusions. The results generated and conclusions drawn enable us to propose whether the construction of these minature flow devives would be worthwhile.

Declaration

I confirm that this work is my own and the use of material from other sources has been properly and fully acknowledged.

Martyn Taylor, 21-08-2005

Contents

Chapter 1

Introduction and project aims

Materials encountered in industry invariably fall outside of the classical extremes of Newtonian viscous fluids and Hookean elastic solids. When this situation occurs, in the case of fluids, we refer to non-newtonian fluid dynamics. A non-Newtonian fluid is defined to be one whose behaviour cannot be predicted on the basis of the Navier-Stokes equation. Such fluids may or may not possess a memory of past deformation - if they do they are called non-Newtonian viscoelastic fluids [7]. This project involves looking at the flow of these non-Newtonian fluids in different flow geometries and then reducing the length scale of the geometries to a smaller scale, in the region of microns. The motivation for this study arises from scenarios where the volume of material available is limited, this being typical in the biological sciences and medicine.

We begin by discussing the properties and equations for Newtonian and non-Newtonian flows. Various models for the non-Newtonian case are discussed briefly, the main aim being to present the equations for these models, as an

introduction to the field. We then introduce the finite element method: the underlying concepts that will be required in order to understand subsequent, how we adapt the finite element method to solve for viscoelastic flows and the method employed by our modelling software, Femlab. We discuss how Femlab works, exploring its set-up of the problem and the techniques it uses to solve the problem. We then explore 3 different parellel plate geometries, presenting the graphical results from Femlab and interpreting them. This will all be done on a standard length scale, before we look at the scaling of these equations to the micron level.

The specific aim of this project is to address the questions:

> *Do models for the behaviour of the flow of non-Newtonian liquids still hold if we reduce the length scale of the system to the order of microns? If there is any differences, what are they? And are they major, significant differences?*

> *From the studies, which model is best for flow devices? Should we rule any geometries out?*

Chapter 2

Background

2.1 Notation

The following list contains the notation used in this chapter to describe the flow of fluids. It will continue to be used in subsequent chapters where necessary.

ρ - Density of the fluid

v - Velocity

π - Stress tensor

g - Gravitational acceleration

t - Time

$\hat{U}$ - Internal energy per unit mass

q - Heat flux

δ - Unit tensor

μ - Viscosity

τ - Momentum flux tensor

κ - Dilatational viscosity

$\dot{\gamma}$ - Rate of deformation tensor

k - Thermal conductivity

T - Temperature

τ - shear stress D - rate of deformation tensor

2.2 Review of Newtonian Fluid Dynamics

In this introductory chapter we review the equations that describe Newtonian fluid flow. It is a necessary prerequisite as the equations governing the viscoelastic flow will be similar up to the addition of the added complexity arising from the viscoelastic behaviour.

2.2.1 Equations of change

The flow of any fluid is governed by the equations of conservation of mass, momentum and energy. Concerning ourselves first with the equation for conservation of mass, we get the continuity equation, (2.1)

$$\frac{\partial \rho}{\partial t} = -(\nabla \cdot \rho \mathbf{v}) \tag{2.1}$$

If the fluid has a constant density then (2.1) is reduced to (2.2). This is refered to as the continuity equation for incompressible fluids.

$$\nabla \cdot \mathbf{v} = 0 \tag{2.2}$$

The equation of motion (2.3) is derived from the principle of conservation of momentum, where π is the stress tensor.

$$\frac{\partial}{\partial t}\rho \mathbf{v} = -[\nabla \cdot \rho \mathbf{v}\mathbf{v}] - [\nabla \cdot \pi] + \rho \mathbf{g} \tag{2.3}$$

The final equation, the internal energy equation, is derived from the conservation of energy. Making the assumption that the stress tensor is symmetric we get

$$\frac{\partial}{\partial t}\rho\hat{U} = -(\nabla \cdot \hat{U}\mathbf{v}) - (\nabla \cdot \mathbf{q}) - (\nabla \cdot [\pi \cdot \mathbf{v}]) + \mathbf{v}[\nabla \cdot \pi] \tag{2.4}$$

where $\hat{U}$ represents the internal energy per unit mass and $\mathbf{q}$ represents the heat flux.

2.2.2 Transport properties

The equations in the previous section are valid for any type of fluid. In this section we specilize these equations for Newtonian fluids to obtain the classical equations of hydrodynamics.

The generalized form of the shearing motion of an arbitrary, time-dependent flow is given in (2.5). For definitions of all the terms see the notation page at the front of the dissertation.

$$\pi = p\delta + \tau = p\delta - \mu[\nabla v + (\nabla v)^{\dagger}] + (\frac{2}{3}\mu - \kappa)(\nabla \cdot v)\delta \tag{2.5}$$

For all fluids the density, ρ, is dependent on the temperature and pressure. However, it is often convenient to make the assumption that for liquids the density is constant, i.e. we have an incompressible fluid. Using this assumption, an assumption we will continue throughout the dissertation unless otherwise stated, and letting $\dot{\gamma} = \nabla v + (\nabla v)^{\dagger}$ we get a simplified form of (2.5)

$$\pi = p\delta + \tau = p\delta + \mu\dot{\gamma} \tag{2.6}$$

We use Fourier's law of heat conduction to define the heat flux, $\mathbf{q}$,

$$\mathbf{q} = -k\nabla T \tag{2.7}$$

We are now in a position to express the equations of change using these new definitions. The equation of continuity, (2.2), remains the same, and can be

interpreted physically as saying that within a small fixed volume of fluid there will be no net rate addition of mass.

The equation of motion, (2.3), is now expressed as (2.8) and states that the mass multiplied by the acceleration of a fluid element is equal to the sum of the pressure, viscous and gravitational forces acting on this element.

$$\rho[\frac{\partial \mathbf{v}}{\partial t} + (\mathbf{v} \cdot \nabla)\mathbf{v}] = -\nabla p + \mu \nabla^2 \mathbf{v} + \rho \mathbf{g} \tag{2.8}$$

The energy equation relates the change in the temperature of the fluid element as it moves with the fluid due to heat conduction and viscous heating. It can be expressed as

$$\rho \hat{C}_p[\frac{\partial T}{\partial t} + (\mathbf{v} \cdot \nabla)T] = k\nabla^2 T + \frac{1}{2}\mu(\dot{\gamma}[\nabla \cdot [\dot{\gamma} \cdot \dot{\gamma}] - \dot{\gamma}[\nabla \cdot \dot{\gamma}]) \tag{2.9}$$

where $\hat{C}_p$ is the heat capacity at constant pressure per unit mass.

There are many experiments, such as the rod-climbing effect and the Quell-effect, that demonstrate that non-Newtonian fluids cannot be described using Newton's law of viscocity. In Figure 1.1 we illustrate this with the rod-climbing effect. The beaker in (a) contains a Newtonian liquid which shows a vortex. The beaker in (b) contains a non-Newtonian liquid which climbs the rod [1].

In the next section we look at ways of properly describing these non-Newtonian fluids.

2.3 Non-Newtonian Fluids

In this section we introduce non-Newtonian fluids - this section effectively serves as a background on the fluids we will be studing. When we refer to viscoelastic fluids we are refering to a special type of non-Newtonian fluids. The term

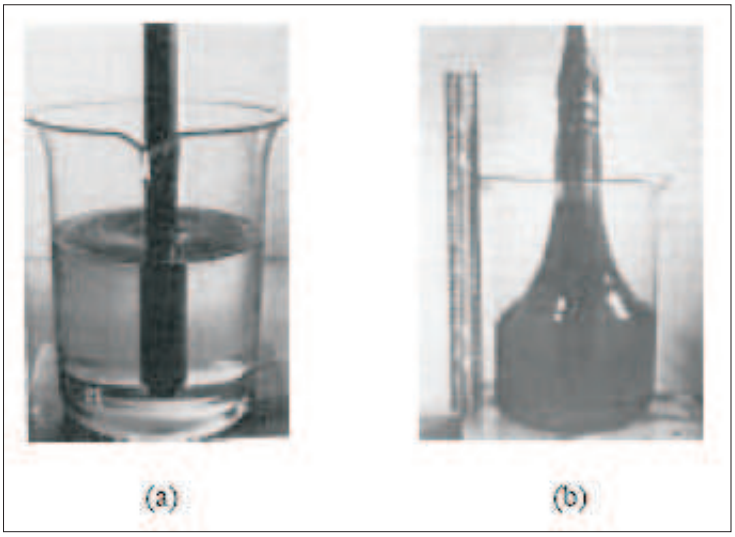

Figure 2.1: Rod-climbing effect

viscoelastic is used as the fluids have both viscous and elastic properties. By using the term elastic we refer to a material that has the ability to return to a previous, unique shape - in a sense it has a memory. We look at the standard flow patterns used in characterizing viscoelastic fluids and look at the material functions. We consider two standard kinds of flow: shear and shearfree flows.

2.3.1 Shear flows

A shear flow is given by the velocity field

$$v_x = \dot{\gamma_{yx}} y \qquad v_y = v_z = 0 \tag{2.10}$$

where $\dot{\gamma_{yx}}$ is the velocity gradient. We obtain the shear rate if we take the absolute value of $\dot{\gamma_{yx}}$. In the case where the shear rate is independent of time we get what is known as steady shear flow, a typical characteristic of this flow being the distance between two particles, l, initially at distance l_o apart, being

given by

$$l = l_o\sqrt{1 + (\dot{\gamma}\Delta t)^2} \approx l_o\dot{\gamma}\Delta t \tag{2.11}$$

We next present the stress tensor, π. The most general form of the stress tensor is

$$\pi = p\delta + \tau = \begin{pmatrix} p + \tau_{xx} & \tau_{yx} & 0 \\ \tau_{yx} & p + \tau_{yy} & 0 \\ 0 & 0 & p + \tau_{zz} \end{pmatrix} \tag{2.12}$$

We define the non-Newtonian viscosity as

$$\tau_{yx} = -\eta(\dot{\gamma})\dot{\gamma_y}x \tag{2.13}$$

Similarly we can define the normal stress coefficients Ψ_1 and Ψ_2

$$\tau_{xx} - \tau_{yy} = -\Psi_1(\dot{\gamma})\dot{\gamma_{yx}}^2 \qquad \tau_{yy} - \tau_{zz} = -\Psi_2(\dot{\gamma})\dot{\gamma_{yx}}^2 \tag{2.14}$$

We now move on to discussing these properties for shearfree flow.

2.3.2 Shearfree flows

Simple shearfree flows are given by the velocity field

$$v_x = -\frac{1}{2}\dot{\epsilon}(1+b)x \qquad v_y = -\frac{1}{2}\dot{\epsilon}y \qquad v_z = \epsilon z \tag{2.15}$$

where $0 \leq b \leq 1$ and $\dot{\epsilon}$ is the elongation rate. The particular case of $b = 0$, $\dot{\epsilon} > 0$ is elongational flow and will be discussed in more detail shortly. For steady shearfree flow the elongation rate is independent of time. For steady shearfree flows we have the characteristic that, after time Δt,

$$l = l_o e^{\dot{\epsilon}\Delta t} \tag{2.16}$$

where l and l_o are defined as for the steady shear flow case.

The stress tensor for shearfree flow, (2.17), is similar to that for shear flow except that the off-diagonal components are all zero

$$\pi = p\delta + \tau = \begin{pmatrix} p+\tau_{xx} & 0 & 0 \\ 0 & p+\tau_{yy} & 0 \\ 0 & 0 & p+\tau_{zz} \end{pmatrix} \tag{2.17}$$

If we assume that the flow is isotropic, the material functions and stresses are only dependent on $\dot{\epsilon}(t)$ and the parameter b. We define two viscosity functions $\bar{\eta_1}$ and $\bar{\eta_2}$ as

$$\tau_{zz} - \tau_{xx} = -\bar{\eta_1}(\dot{\epsilon}, b)\dot{\epsilon} \qquad \tau_{yy} - \tau_{xx} = -\bar{\eta_2}(\dot{\epsilon}, b)\dot{\epsilon} \tag{2.18}$$

For the case where $b = 0$, $\bar{\eta_2} = 0$ and $\bar{\eta_1} = \bar{\eta}$, where $\bar{\eta}$ is the elongational viscosity, and taking $\dot{\epsilon} > 0$ we have elongational flow.

Having discussed shear and shearfree flows we now move on to discuss linear viscoelastic fluids and discuss some of the models that have been devised to describe these flows.

2.4 Linear Viscoelastic fluids

The main aim of this section is to show how the ideas of viscosity and elasticity can be combined to derive a single constitutive equation describing the viscoelastic effects of viscoelastic liquids. We look at a variety of different models that have been derived to describe the flow for completeness for the reader, but will be only concentrating on one of these models in future work.

2.4.1 The Maxwell model's

The Maxwell model

Bird et al [1] discuss Maxwell's model as being the first attempt to obtain a

viscoelastic constitutive equation, which was proposed in the late 19^{th} century. Maxwell believed gases to be viscoelastic, which was his motivation for developing his model. His model claimed that all fluids that are both viscous and elastic could be described using (2.19). For steady state flow this equation simplifies to one describing the motion of a Newtonian fluid with viscosity μ.

$$\tau_{yx} + \frac{\mu}{G}\frac{\partial \tau_{yx}}{\partial t} = -\mu\dot{\gamma}_{yx} \tag{2.19}$$

It has been recognized that these classical constitutive equations have their limitations. Many systems require much more complex descriptions. It is this limitation that leads us to look at some alternative forms of the Maxwell model. We generalize to arbitrary, small displacement flows by putting the equation in tensor form. We introduce some new constants, η_0, the zero-shear-rate viscosity to replace μ, and we replace $\frac{\mu}{G}$ by λ_1, which is called the relaxation time. The Maxwell equation becomes a differential equation for τ,

$$\tau + \lambda_1\frac{\partial}{\partial t}\tau = -\eta_0\dot{\gamma} \tag{2.20}$$

This equation is easy to solve for τ as it is a first order, linear equation for τ as a function of time. It can be integrated once to give

$$\tau(t) = e^{-\frac{t}{\lambda_1}}\Big[\int\Big(-\frac{\eta_0}{\lambda_1}\dot{\gamma}(t)\Big)e^{\frac{t}{\lambda_1}}dt + \mathbf{k}\Big] \tag{2.21}$$

We wish to affix limits to the integral. The upper limit is simply the time we are currently at in the flow, which we will assign as t'. The lower limit we will take as $-\infty$. It is an arbitrary choice - a choice of a different lower limit would result in a different value of constant, $\mathbf{k}$. Using l'Hopital's rule we get that the stress is finite at $-\infty$ as long as $\dot{\gamma}(-\infty)$ is finite, and hence we get the Maxwell constitutive equation in the form

$$\tau(t') = -\int_{-\infty}^{t'}\Big[\frac{\eta_0}{\lambda_1}e^{-(t'-t)/\lambda_1}\Big]\dot{\gamma}(t)dt \tag{2.22}$$

The quantity $\Big[\frac{\eta_0}{\lambda_1}e^{-(t'-t)/\lambda_1}\Big]$ is known as the relaxation modulus for the Maxwell fluid. The relaxation modulus, denoted by G, relates the time dependent strain

in the system to the stress [2]. If we take the Laplace transform of the relaxation modulus, (2.23), we get the storage and loss moduli. These are respectively the real ($G'(\omega)$) and imagnary ($G''(\omega)$) parts of the complex relaxation modulus, $G^*(\omega)$. These quanities represent the elastic and dissipative components of the complex viscoelastic behaviour [2].

$$G^*(\omega) = i\omega \int_0^\infty G(t) e^{-i\omega t} dt \tag{2.23}$$

If we perform an integration by parts on the current Maxwell model we get

$$\tau(t') = \int_{-\infty}^{t} \Big[\frac{\eta_0}{{\lambda_1}^2} e^{-(t'-t)/\lambda_1} \Big] \gamma(t', t) dt' \tag{2.24}$$

The quantity within the square brackets is known as the memory function for the Maxwell fluid. In this form the Maxwell model states that the present time t' depends on the history of the strain for all past times, t, in the interval $[-\infty, t']$. The exponential term in the integrand represents the fading memory [1].
All three forms of the Maxwell equation are the same provided that $\dot{\gamma}$ is finite at $t = -\infty$ and the displacement gradients are infinitesimally small.

The Upper convected Maxwell (UCM) model

When the Maxwell model is generalised to arbitrary flows by putting it in tensor form and the upper convected time derivative is used in place of the partial time derivative, we obtain the Upper convected Maxwell model. The constitutive equation for this model is given below.

$$\lambda \tau^{\nabla} + \tau = 2\eta_0 \mathbf{D} \tag{2.25}$$

where λ and η_0 are the relaxation time of the fluid and zero-shear-rate viscosity respectively, $\mathbf{D}$ is the rate of deformation tensor given here as: $\mathbf{D} = \frac{1}{2}(\nabla u + \nabla u^\dagger)$ and τ^{∇} is the upper convected time derivative of the stress tensor, defined by $\tau^{\nabla} = \frac{\partial \tau}{\partial t} + (u \cdot \nabla)\tau - \nabla u \cdot \tau - \tau \cdot (\nabla u)^\dagger$, where $\dagger$ represents the transpose.

The Generalized Maxwell Model

If we construct a superposition of Maxwell models we can obtain another model for the Maxwell flow. If we proceed by obtaining the constitutive equation, (2.26), and then integrating once to obtain (2.27), and then finally integrate (2.27) by parts to get (2.28), we obtain the following set of equations.

$$\tau(t') = \sum_{k=1}^{\infty} \tau_k(t') \qquad \tau_k + \lambda_k \frac{\partial}{\partial t'}\tau_k = -\eta_k \dot{\gamma} \tag{2.26}$$

$$\tau(t') = -\int_{-\infty}^{t'} \Big[\sum_{k=1}^{\infty} \frac{\eta_k}{\lambda_k} e^{-(t'-t)/\lambda_k}\Big] \dot{\gamma}(t) dt \tag{2.27}$$

$$\tau(t') = \int_{-\infty}^{t'} \Big[\sum_{k=1}^{\infty} \frac{\eta_k}{{\lambda_k}^2} e^{-(t'-t)/\lambda_k}\Big] \gamma(t', t) dt' \tag{2.28}$$

The convention that $\lambda_1 > \lambda_2 > ..... > \lambda_k > .....$ is employed. This model can contain an infinite spectrum of relaxation times and viscosities, however setting $\lambda_k = 0$ and $\eta_k = 0$ for some k greater than K finite we can reduce the spectrum to a finite number.

2.4.2 The Jeffreys Model

The Maxwell model is a linear relation betweem τ and $\dot{\gamma}$. However, it is easy to invent other linear relations between quantities. In order to obtain the Jeffrey model we include the time derivative of $\dot{\gamma}$ and get the constitutive equation, (2.29), containing two time constants, λ_1, the relaxation time, and λ_2, the retardation time.

$$\tau + \lambda_1 \frac{\partial \tau}{\partial t} = -\eta_0 \Big(\dot{\gamma} + \lambda_2 \frac{\partial \dot{\gamma}}{\partial t}\Big) \tag{2.29}$$

This model was put forward by H.Jeffreys in 1929. If we integrate (2.29) as a first order differential equation, using the initial condition that τ should be finite at $t = -\infty$, we find that, provided both $\dot{\gamma}$ and $\frac{\partial \dot{\gamma}}{\partial t}$ are finite at $t = -\infty$ [1],

$$\tau(t) = -\int_{-\infty}^{t} \frac{\eta_0}{\lambda_1}\Big(1 - \frac{\lambda_2}{\lambda_1}\Big)e^{-(t-t')/\lambda_1}\dot{\gamma}(t')dt' - \frac{\eta_0\lambda_2}{\lambda_1}\dot{\gamma}(t) \tag{2.30}$$

In order to determine the relaxation modulus we use the Dirac delta function and the definition $\delta(x) = \lim_{n\to\infty}\sqrt{\frac{n}{\pi}}e^{-nx^2}$ [3]

$$\tau(t) = -\int_{-\infty}^{t} \Big[\frac{\eta_0}{\lambda_1}\Big(1 - \frac{\lambda_2}{\lambda_1}\Big)e^{-(t-t')/\lambda_1} + 2\frac{\eta_0\lambda_2}{\lambda_1}\delta(t-t')\Big]\dot{\gamma}(t')dt' \tag{2.31}$$

The relaxation modulus for Jeffreys Model is given by the quantity inside the square brackets. To obtain the memory function we preceed as with the Maxwell model, using integration by parts on (2.31).

$$\tau(t) = \int_{-\infty}^{t} \Big[\frac{\eta_0}{{\lambda_1}^2}\Big(1 - \frac{\lambda_2}{\lambda_1}\Big)e^{-(t-t')/\lambda_1} + \frac{2\eta_0\lambda_2}{\lambda_1}\frac{\partial}{\partial t'}\delta(t-t')\Big]\gamma(t,t')dt' \tag{2.32}$$

The memory function is again the function within the square brackets.

2.4.3 The Oldroyd-B model

When the partial time derivatives in the Jeffreys Model are replaced by upper convected time derivatives we obtain the quasi-linear Oldroyd-B model. The constitutive equation for this model is given below.

$$\mathbf{T} + \lambda_1\mathbf{T}^{\nabla} = 2\eta_0(\mathbf{D} + \lambda_2\mathbf{D}^{\nabla}) \tag{2.33}$$

where λ_1, λ_2, η and $\mathbf{D}$ are as before with the UCM model. $\mathbf{T} = \tau + 2\eta_2\mathbf{D}$ is the extra stress tensor where τ satisfies the UCM model $\lambda_1\tau^{\nabla} + \tau = 2\eta_1\mathbf{D}$, with η_1 and η_2 defined by $\eta = \eta_1 + \eta_2$, $\lambda_2 = \frac{\eta_2}{\eta}\lambda_1$.

The Oldroyd-B model is equivalent to a linear combination of the UCM model and the Newtonian model. If the relaxation and retardation time are equal, then the model is equivalent to the Newtonian model, where the viscosity of the Newtonian fluid is equal to the zero-shear-rate viscosity of the Oldroyd-B fluid. If the retardation time is equal to zero, we retrive the UCM model.

2.4.4 The General Linear Viscoelastic model

If we compare the equations for the the Maxwell model, (2.22), the Jeffrey's model, (2.31), and the Generalized Maxwell model, (2.27), we notice that they are all integrals over the relaxation modulus multiplied by the rate of deformation tensor. An equation that includes all three of these models is known as the General Linear Viscoelastic model. It can be written in two equivalent forms, (2.34) and (2.35), where the relaxation modulus is denoted by $G(t'-t)$ and $M(t'-t)$ is the memory function and is equal to $\frac{\partial G(t'-t)}{\partial t}$.

$$\tau = -\int_{-\infty}^{t'} G(t'-t)\dot{\gamma}(t)dt \tag{2.34}$$

$$\tau = \int_{-\infty}^{t'} M(t'-t)\gamma(t',t)dt \tag{2.35}$$

The functions $G(t'-t)$ and $M(t'-t)$ are positive, monotonically decreasing functions, tending to zero as $t'-t$ tends to infinity. Viscoelastic fluids which have this property are refered to as having a fading memory.

Having given brief descriptions of Newtonian and non-Newtonian fluids and investigated the different models describing viscoelastic flow we next proceed to give the background behind the finite element method. Femlab, the software package we will use to model the flows of the viscoelastic fluids, uses the finite element technique to solve the systems of equations. It is therefore important to have an understanding of the underlying concepts behind the finite element method, before discussing how this method is adapted for viscoelastic flows and using it to provide us with our numerical solutions in the later chapters.

Chapter 3

Background of the Finite element method

In numerical analysis the finite element method is used to solve partial differential equations approximately. The following quote gives a concise summary of the fimite element method:

> *The finite element method is a general technique to build finite dimensional subspaces of a Hilbert space V in order to apply the Rayleigh-Ritz or Galerkin method to a variational problem.* [4],[5]

The finite element method was proposed in a paper by Richard Courant in the early 1940's, although the historical roots of the method can be traced back to the earlier works of Galerkin in 1915. Unfortunately, the relevance of Courant's work was not recognized at the time and the idea was forgotten. The idea was rediscovered in the early 1950's by engineers but the mathematical analysis began only a decade later and has since been developed into one of the most powerful techniques for numerical simulation of differential equations [6].

The finite element technique, unlike finite difference techniques which seek to approximate the unknown analytical solution to a differential equation at a finite number of grid points in the computational domain, supplies an approximation to the analytic solution in the form of a piecewise polynomial, defined over the entire computational domain [6]. We shall look at two techniques for the construction of finite element approximations: the *Rayleigh-Ritz principle* and the *Galerkin principle*. Before beginning this, however, we look at some fundamental, preliminary concepts necessary to understand the finer details of the finite element method.

3.1 Preliminary concepts

It is important to have a basic understanding of the concepts that are discussed in the following subsections to understand the underlying theory for the finite element method.

3.1.1 Classification of Partial Differential Equations (PDEs)

We consider a general, linear, second order PDE in two indepent variables x and y:

$$Lu = \alpha u_x x + \beta u_x y + \chi u_y y + \delta u_x + \epsilon u_y + \phi u = \zeta$$

where $\alpha = \alpha(x, y)$, $\beta = \beta(x, y)$, ... and $u(x, y)$ is the dependent variable. The subscript indicates differentation by that variable. The prinicipal part of the symbol of L is:

$$L^p(x, y; i\xi, i\eta) = -\alpha\xi^2 - \beta\xi\eta - \chi\eta^2$$

The equation is said to be

- Hyperbolic if $\beta^2 > 4\alpha\chi$
- Parabolic if $\beta^2 = 4\alpha\chi$

- Elliptic if $\beta^2 < 4\alpha\chi$

3.1.2 Sobolev spaces

Definition 2.1.2.1 For $k \in \Re^{>0}$, we define the **Sobolev space** $H^k(a,b)$ as the set of real valued functions v defined on $[a,b]$ such that v and all of its derivatives of order up to and including $k-1$ are absolutely continuous on $[a,b]$ and

$$v^{(k)} = \frac{\partial^k v}{\partial x^k} \in L^2(a,b)$$

Here $L^2(a,b)$ denotes the set of all functions defined on (a,b) such that

$$\|v\|_2 = \|v\|_{L^2(a,b)} = \Big(\int_a^b |v(x)|^2 \, dx \Big)^{1/2}$$

is finite. We equip $H^k(a,b)$ with the **Sobolev norm**

$$\|v\|_{H^k(a,b)} = \Big(\sum_{m=0}^{k} \left\| v^{(m)} \right\|^2_{L^2(a,b)} \Big)^{1/2}$$

Definition taken from [6]

Particularly relevant Sobolev spaces for the next section are the $H^1(a,b)$ and the $H^2(a,b)$ (corresponding to the $k=1$ and $k=2$ case respectively). For the imposition of boundary conditions we need varients of the space $H^1(a,b)$.

Definition 2.1.2.2 (i) Given $A, B \in \Re$, $H^1_E(a,b)$ will denote the set of all functions $v \in H^1(a,b)$ such that $v(a) = A$ and $v(b) = B$.
(ii) $H^1_0(a,b)$ will signify the set of all functions $v \in H^1(a,b)$ such that $v(a) = 0$ and $v(b) = 0$.

Definition taken from [6]

We are now in a position to state the Rayleigh-Ritz and Galrekin principles.

3.2 The finite element method

The finite element method involves solving an equation by approximating continuous functions on a mesh. The two ways to formulate the finite element problem are the Rayleigh-Ritz method, which is based on finding an approximate solution to the variational problem, and the Galerkin method, which does not require the existence of a variational formulation [5].

Both methods require an approximate solution of the form

$$U(x) \approx \sum_i U_i \phi_i(x) \tag{3.1}$$

where $U(x)$ is the function to be approximated, U_i are nodal parameters and ϕ_i are the basis functions. The basis functions are constructed element by element by shape functions. The example in Fig 2.1 uses triangles with the triangle points serving as nodes. The test functions will be triangle-wise linear fuctions which are continuous over the triangles edges.

We introduce the notation ϕ_i^e to represent ϕ restricted to a specific element, denoted e. This gives us that the ϕ_i is a sum across all elements of ϕ_i^e. In order to make the integration easier, we can map each element onto a parent element, denoted P. In the case of two dimensions the integral given by equation (3.2) becomes (3.3).

$$\int\int_\Omega f(U)\ dx\ dy \tag{3.2}$$

$$\sum \int\int_P f(U)\ J\ dp\ dq \tag{3.3}$$

The J referenced in equation (3.3) represents the Jacobian of the transformation from the element in (x, y) space to the element in the parent space, (p, q).

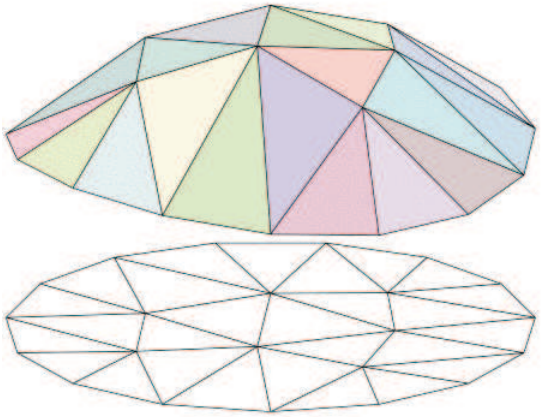

Figure 3.1: Finite element representation

3.2.1 The Rayleigh-Ritz and Galerkin method's

Let us define the functional $\varsigma : H_e^1(a,b) \rightarrow \Re$ and consider the variational problem:

$$\textit{Find } u \in H_E^1(a,b) \textit{ such that } \varsigma(u) = min_{\omega \in H_E^1(a,b)} \varsigma(\omega).$$

This is known as the **Rayleigh-Ritz principle**. If an approximate solution to this variational principle is required, then if we use the form given by equation (3.1) and minimise over the subspace that is spanned by ϕ_i we get the approximate problem (3.4). This method produces one equation for each of the parameters that are not already specified from the boundary conditions.

$$\frac{\partial}{\partial U_i} \varsigma\Big(\sum_j U_j \phi_j \Big) = 0 \qquad i = 1, ...N \tag{3.4}$$

If we now consider the problem:

Problem *Find $u \in V$ such that $Au = f$ where A is a linear differential operator.*

Any function u that satisfies this problem is refered to as the strong solution of the problem. If instead the function u only satisfies the following Theorem (Galerkin's principle) then it is refered to as being the weak solution of our problem.

Theorem 2.2.1.1 A function u in $H_E^1(a,b)$ minimises $\varsigma(\cdot)$ over $H_E^1(a,b)$ if and only if

$$A(u,v) = \langle f, v \rangle \qquad \forall v \in H_0^1(a,b) \tag{3.5}$$

and

$$A(w,v) = A(v,w) \qquad \forall w, v \in H^1(a,b)$$

$\diamondsuit$

Theorem taken from [6]

Definition 2.2.1.2 If a function $u \in H_E^1(a,b)$ satisfies Theorem 2.2.1.1 then it is called a weak solution to the boundary value problem in question. In this case the Galerkin principle is refered to as the **weak formulation** of the boundary value problem.

Definition taken from [6]

The finite element method is based on constructing approximate solutions u^h to the problem. We can choose a conforming approximation space $V_E^h \in H_E^1(a,b)$ (a finite dimensional subset). Often V_E^h will contain polynomials of a certain degree. The discrete Galerkin approximation to our problem can now be expressed

Theorem 2.2.1.3 A function $u^h \in V_E^h$ minimises $\varsigma(\cdot)$ over V_E^h if and only if

$$A(u^h, v^h) = \langle f, v^h \rangle \qquad \forall v^h \in S_0^h \tag{3.6}$$

where

$$S_0^h = \left\{ v^h \in H_0^1(a,b) : v^h(x) = \sum_{i=1}^{n-1} v_i \phi_i(x) \right\}$$

with $(v_1, v_2, ..., v_{n-1}) \in \Re^{n-1}$.

$\diamondsuit$

Theorem taken from [6]

3.3 Mixed Finite Elements

[5] and [8] both discuss Mixed Finite Element methods. If we consider the problem:

Find $u \in V$ such that

$$-\nabla . A(x) \nabla u = f \qquad in \qquad \Omega$$

$$u_{\gamma 0} = g_1 \qquad on \qquad D$$

$$A(x) \nabla u . n = g_2 \qquad on \qquad N$$

where Ω is a bounded domain in $\Re^n$ and $D \cup N = \partial\Omega$.

We assume that $A(x)$ is an $n \times n$ positive definite matrix and that the smallest

eigenvalue of $A(x)$ is bounded away from zero uniformly with respect to x. First if we have $g_1 = 0$ we can write our standard variational formulation as a minimisation problem, which is known as the Primal Formulation. We can further transform this Primal Formulation into a Mixed Formulation with $f \in L^2(\Omega)$ and $g_2 = 0$. This is a saddle point problem, so defining

$$a(p,q) = \int_\Omega A^{-1} p.q dx$$

$$b(v,q) = \int_\Omega v \nabla .q dx$$

we can write this Mixed Formulation as

$$a(p,q) + b(q,u) = \langle g_1, q.n \rangle \qquad \forall q \in H_{0,N}(div : \Omega)$$

$$b(p,v) = -\int_\Omega f v dx \qquad \forall v \in L^2(\Omega)$$

If the subscript h indicates a finite element approximation to that quantity, the discrete problem may now be written as:

Find $(p_h, u_h) \in V_h \times Q_h$ *such that:*

$$a(p_h, q_h) + b(q_h, u_h) = \langle \tilde{g}, q_h \rangle \qquad \forall q_h \in V_h$$

$$b(p_h, v_h) + \left\langle \tilde{f}, v_h \right\rangle = 0 \qquad \forall v_h \in Q_h$$

where $\tilde{f}$ *and* $\tilde{g}$ *may include non-homogeneous boundary conditions:*

$$\langle \tilde{g}, q \rangle = \langle g_1, q.n \rangle - a(\tilde{q}, g)$$

$$\left\langle \tilde{f}, v \right\rangle = \int_\Omega f v dx + b(\tilde{q}, v)$$

$$A^{-1}\tilde{q}.n = g_2 \qquad onN.$$

3.4 Finite Element methods for solving viscoelastic flows

As was discussed in the previous section, the finite element method is a technique for approximating the solution to equations. In the remainder of this

chapter we explore the use of finite elememt techniques for the solving of viscoelastic flow. We consider an Oldroyd B fluid model, as discussed in section 1.3.3. When we solve for viscoelastic flows it is necessary for the stress to be calculated explicity and the nature of the partial differential equations to be considered. The reason for this comes from the term $v.\nabla\tau$ in the equation for the upper convected derivative, defined previously as T^{∇}. This term causes a mixed character of the governing equations, with them exhibiting both elliptic and hyperbolic behaviour. The result of this mixed behaviour causes the Galerkin method to become unstable [5]. There have been a number of techniques produced for stabilizing the approximation. These will be discussed in detail in the remainder of this section.

3.4.1 The Streamline Upwind Petrov-Galerkin technique

The Streamline Upwind Petrov-Galerkin technique uses a different test and trial space for the stress approximation [5]. We can define this new test space, $\widetilde{S_h}$ in terms of the trial space T_h by the following:

$$\widetilde{S_h} = S_h + \hat{\kappa}\mathbf{v^*}.\nabla S_h \qquad \forall S_h \in T_h$$

$$\mathbf{v^*} = \frac{\mathbf{v}}{v.v}$$

$$\hat{\kappa} = \frac{\hat{\xi}v_\xi + \hat{\eta}v_\eta}{\kappa}$$

$$v_\xi = v_0.h_\xi$$

$$v_\eta = v_0.h_\eta$$

where v_0 is the velocity at the centre of a quadrilateral in (ξ, η) space, h_ξ and h_η are the elements diameters in the respective directions, $\hat{\xi}$ and $\hat{\eta}$ are based on the directional Péclet numbers and κ is problem dependent.

Equations taken from [5].

It was found by Marchal and Crochet that the SUPG method gives satisfactory results provided the velocity field is specified, but it was not suffucient to solve the set of coupled equations. Later work showed that singularities in specific geometries was the problem behind the production of these poor results. The SUPG method was found to give stable and accurate results for flows of an UCM fluid through smooth geometries.

3.4.2 EVSS Technique

The stress variable τ_h is replaced by σ_h, which is defined as:

$$\sigma_h = \tau_h - 2\eta_p \mathbf{D}(v_h)$$

and σ_h is then solved for when we use the EVSS technique. In order to stabilize the technique further we can also solve for $\mathbf{D}$ as a seperate variable.

3.4.3 DEVSS Technique

If we add an elliptic term to our momentum equation in order to stabilize the system of coupled equations we obtain the DEVSS technique. Let us consider

$$\alpha \nabla^2 \mathbf{v}_h - \alpha \nabla . 2\mathbf{D}_h$$

and add this to the left hand side of the momentum equation. $\mathbf{D}_h$ is the L_2 projection of the tensor $\mathbf{D}$ and α is a positive constant. In the discrete problem, the discrete rate of deformation tensor is next solved for, treating it as an extra variable. We thus add the follwing equation to our problem

$$\int_\Omega (2\mathbf{D}_h - \nabla^2 \mathbf{v}_h) : G_h d\Omega = 0 \qquad \forall G_h \in \Theta_h$$

3.4.4 Artifical Diffusion/Streamline Upwind Technique

In order to stabilize the viscoelastic approximations, an artifical diffusivity tensor can be added to the equation. This technique allows the stress to diffuse

along the streamlines. Whilst this diffusion occurs no cross wind diffusion takes place. This technique allowed Marchal and Crochet [9] to suppress the oscillations present in the SUPG solutions. Further calculations also showed that this technique is highly stable, however inaccuracies in the boundary layer are serverly increased. Inccuracies are also increased in regions where the magnitude of the second derivative of the stress is important.

3.4.5 Technique comparison

[5] compared three techniques in the context of a 1-D model of Maxwell flow (section 2.4.1). These were the Streamline Upwind Technique (SU), SUPG and EVSS techniques. It was found that SU method was stable for both smooth and non-smooth problems, but had a slow rate of convergence for the stress field. The SUPG method was stable only for smooth problems and the EVSS technique was stable for both smooth and non-smoth problems, but its advantages were diminshed in the proximatey of a singularity.

The same techniques were employed upon a 2-D problem, using the UCM model. The EVSS technique showed stable approximations to all problems, but was extremely expensive computationally. The SU technique was shown to be less predictable then the other techniques and the SUPG technique failed in regions which possessed singularities.

Chapter 4

Numerical simulation

In order to solve our problem for viscoelastic flow we use Femlab to generate the results. Before proceeding to solve the equations we first give an introductory discussion about Femlab, how it solves the fininte element equations and its solver functions.

4.1 Solving of Finite element equations

As discussed in the previous chapter we have shown how the variational formulations form the basis of the finite element method. In this section we discuss how our software solves the finite element equations. Furthermore we give a discussion of the streamline-diffusion method which allows us to obtain stable discretizations of hyperbolic or semi-hyperbolic problems (the latter being the case we will have to deal with).

We consider a domain Ω on which we have the set of linear functions on the triangulation ω of this domain. Upon studing a PDE of the coefficient form in Femlab, multiplying this PDE by a test function, v, integrating over Ω and finally integrating the result by parts (using Green's formula) we obtain the

variational form of our PDE:

Find u_k and λ_m such that:

$$\int_\Omega \Big(\Big(c_{lkji} \frac{\partial u_k}{\partial x_i} + \alpha_{lkj} u_k \Big) \frac{\partial v}{\partial x_j} + \Big(d_{a_l k} \frac{\partial u_k}{\partial t} + \beta_{lki} \frac{\partial u_k}{\partial x_i} + a_{lk} u_k \Big) v \Big) dx +$$

$$\int_{\partial\Omega} q_{lk} u_k v ds = \int_\Omega \Big(\gamma_{lj} \frac{\partial v}{\partial x_j} + f_l v \Big) dx + \int_{\partial\Omega} (g_l - h_{ml} \lambda_m) v ds$$

$$\int_{\partial\Omega} \mu h_{mk} u_k ds = \int_{\partial\Omega} \mu r_m ds$$

$\forall\ v$, μ, $l = 1...N$ and $m = 1...M$.

μ is the test function for the boundary equations. This equation is known as the *weak form.*

We approximate u and λ respectively by,

$$U(x) = \sum_{I=1}^{N_p} \sum_{k=1}^{N} U_{I,k} \phi_I(x) \qquad \Lambda(x) = \sum_{K=1}^{N_c} \sum_{L=1}^{n} \sum_{m=1}^{M} \Lambda_{K,L,m} \delta_{K,L}(x)$$

ϕ_I is 0 at all node points in the triangulation except for node I. $\Phi_{K,L}$ is the delta function at a vertex K on a boundary element L. By using the test functions, ϕ_J and $\delta_{K,L}$, on the weak form of the PDE we obtain the following:

$$\int_\omega \Big(c_{lkji} U_{I,k} \frac{\partial \phi_I}{\partial x_i} + \alpha_{lkj} U_{I,k} \phi_I \Big) \frac{\partial \phi_J}{\partial x_j} dx + \int_\omega \Big(d_{a_{lk}} \frac{\partial U_{I,k}}{\partial t} \phi_I + \beta_{lki} U_{I,k} \frac{\partial \phi_I}{partial x_i} + a_{lk} U_{I,k} \phi_I \Big) \phi_j$$

$$+ \int_{\partial\omega} q_{lk} U_{I,k} \phi_I \phi_J ds = \int_\Omega \Big(\gamma_{lj} \frac{\partial \phi_J}{\partial x_j} + f_I \phi_J \Big) dx + \int_{\partial\omega} (g_l - h_{ml} \Lambda_{K,L,m} \Phi_{K,L}) \phi_J ds$$

$$\forall\ J,\ l$$

and

$$\int_{\partial\omega} h_{mk} U_{I,k} \phi I \Phi_{K,L} ds = \int_{\partial\omega} r_m \delta_{K,L} ds$$

$$\forall\ K,\ L,\ m$$

From the above equations we obtain a system of equations for $U_{I,k}$ and $\Lambda_{K,L,m}$. The coefficients for this system of equations is given by the following matrices

$$DA_{(J,l),(I,k)} = \int_\omega d_{alk} \phi_I \phi_J dx \qquad C_{(J,l),(I,k)} = \int_\omega c_{lkji} \frac{\partial \phi_I}{\partial x_i} \frac{\partial \phi_J}{\partial x_j} dx$$

$$AL_{(J,l),(I,k)} = \int_\omega \alpha_{lkj}\phi_I \frac{\partial \phi_J}{\partial x_j} dx \qquad BE_{(J,l),(I,k)} = \int_\omega \beta_{lki} \frac{\partial \phi_I}{\partial x_i} \phi_J dx$$

$$A_{(J,l),(I,k)} = \int_\omega a_{lk}\phi_I\phi_J dx \qquad Q_{(J,l),(I,k)} = \int_{\partial\omega} q_{lk}\phi_I\phi_J ds$$

$$GA_{(J,l)} = \int_\omega \gamma_{lj} \frac{\partial \phi_J}{\partial x_j} dx \qquad F_{(J,l)} = \int_\omega f_l \phi_J dx$$

$$G_{(J,l)} = \int_{\partial\omega} g_l \phi_J ds \qquad H_{(K,L,m),(I,k)} = \int_{\partial\omega} h_{mk}\phi_I \Phi_{K,L} ds$$

$$R_{(K,L,m)} = \int_{\partial\omega} r_m \Phi_{K,L} ds$$

These integrals are computed using Gauss quadrature within each element. The integrals are computed using the formula

$$\int_\omega f(x)dx \approx \sum_{i=1}^{N_t} \sum_{k=1}^{n_{gp}} f(X(G_k, i))W_k v_i$$

where i runs over all the elements in the domain, k runs over all of the Gauss points in the element, W_k are the Gauss point weights, G_k are the coordinates of the local Gauss points, v_i is the volume of the element i and $X(, i)$ is the conversion function from local to real coordinates for the ith element.

Similarly, we have a formula for the boundary elements, where i runs over all boundary elements, k runs over all the Gauss points on the boundary element and a_i is the area of the ith boundary element.

$$\int_{\partial\omega} f(x)dx \approx \sum_{i=1}^{N_c} \sum_{k=1}^{n_{gp}} f(X(G_k, i))W_k a_i$$

The integrals for the H and R matrices containing the basis functions can be computed exactly.

Using the above to numerically compute the matrices, we end up with the system

$$(C + AL + BE + A + Q)U + H^\dagger \Lambda = GA + F + G$$

$$HU = R$$

where † represents the transpose of the matrix, C, AL, BE, A, Q are $N_pN \times N_PN$ matrices, F, GA, G are N_pN vectors, H is a $N_enM \times N_pN$ matrix and R is a N_enM vector.

We then proceed to use a linear solver to solve this set of equations, which is discussed in a subsequent section. First we discuss the Streamline-Diffusion technique.

4.2 Streamline-Diffusion Stabilization

Unlike elliptic or parabolic problems, hyperbolic problems, or semi-hyperbolic problems as we will be dealing with, have preferential directions (or characteristics) in which the information flows [10]. We must therefore have a means of detecting these characteristics and make use of them, otherwise the discrete scheme will be unstable.

A way to avoid these instabilities is to introduce a diffusive term into the discrete equation. Perturbing the equation has the effect of making the discretization stable, but has the feature of vanishing to zero as the mesh size tends to zero. This technique is refered to as artifical viscosity, and is a standard approach for finite difference and volume schemes. Specially what we need for the stabilization of the hyperbolic/semi-hyperbolic problem is diffusion in the direction of the characteristics only - typically when we add isotropic diffusion, or more specifically a Δu term, we tend to add more diffusion than is actually necessary, something that we do not require or want! In the case of the finite element method, the artifical diffusion is implemented by modifying the form of test function in the variational form. This technique, specified to finite elements, is known as *streamline diffusion*, as in fluid flow problems the artifical viscosity

is needed in the direction of flow (or the streamline) only. In Femlab, the coefficient form of the PDE has the variational form modified by using the test function

$$v + \delta_{k'l'}(\beta_{k'li'} - \alpha_{k'li'})\frac{\partial v}{\partial x_i'}$$

This changes the formulation of the variational form and proceeding as we have before we get a resulting set of matrices which are then added to the original set of equations. The matrices we obtain are

$$DAS_{(J,l),(I,k)} = \int_\omega d_{al'k}\phi_l\delta_{k'l'}(\beta_{k'li'} - \alpha_{k'li'})\frac{\partial \phi_J}{\partial x_{i'}}dx$$

$$CS_{(J,l),(I,k)} = \int_\omega \frac{\partial}{\partial x_j}(c_{l'kji}\frac{\partial \phi_I}{\partial x_i})\delta_{k'l'}(\beta_{k'li'} - \alpha_{k'li'})\frac{\partial \phi_J}{\partial x_{i'}}dx$$

$$ALS_{(J,l),(l,k)} = \int_\omega \frac{\partial}{\partial x_j}(\alpha_{l'kj}\phi_I)\delta_{k'l'}(\beta_{k'li'} - \alpha_{k'li'})\frac{\partial \phi_J}{\partial x_{i'}}dx$$

$$BES_{(J,l),(I,k)} = \int_\omega \beta_{l'ki}\frac{\partial \phi_I}{\partial x_i}\delta_{k'l'}(\beta_{k'li'} - \alpha_{k'li'})\frac{\partial \phi_J}{\partial x_{i'}}dx$$

$$AS_{(J,l),(I,k)} = \int_\omega a_{l'k}\phi_I\delta_{Kl'}(\beta_{k'li'} - \alpha k'li')\frac{\partial \phi_J}{\partial x_{i'}}dx$$

$$GAS_{(J,l)} = \int_\omega \frac{\partial \gamma_{l'j}}{\partial x_j}\delta_{Kl'}(\beta_{k'li'} - \alpha_{k'li'})\frac{\partial \phi_J}{\partial x_{i'}}dx$$

$$FS_{(J,l)} = \int_\omega f_{l'}\delta_{Kl'}(\beta_{k'li'} - \alpha_{k'li'})\frac{\partial \phi_J}{\partial x_{i'}}dx$$

The system of equations are

$$(C{+}AL{+}BE{+}A{+}Q{+}CS{+}ALS{+}BES{+}AS)U{+}H^\dagger\Lambda = GA{+}F{+}G{+}GAS{+}FS$$

$$HU = R$$

CS, ALS, BES and AS are all $NN_p \times NN_p$ matrices and FS and GAS are NN_p vectors.

In the next section we discuss the finite element mesh used by our software.

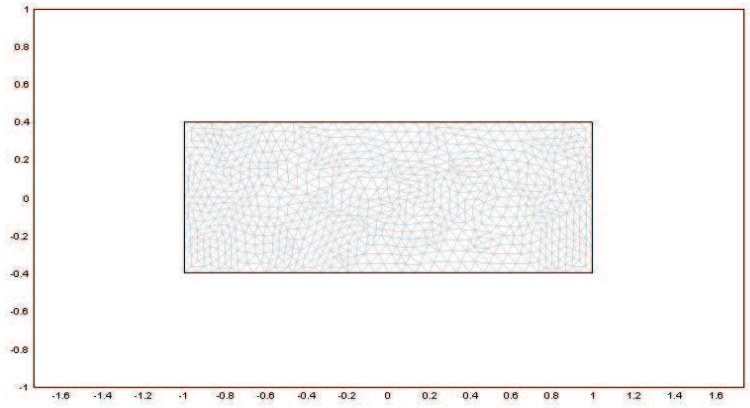

Figure 4.1: Typical mesh for a rectangular domain Ω

4.3 Finite element mesh

If we consider a domain Ω. The Femlab finite element mesh is a triangulaton of Ω (See Figure 3.1). The mesh is represented by what is known as the *FEM* mesh structure, which has three required fields and two optional fields. These are as follows

Required fields:

- *mesh.p* is the node point matrix. It contains the node point coordinates of the mesh. The solution value of component I at node point k is available in $u(k + (I - 1) * N)$ in the *FEM* solution vector u and the corresponding node point co-ordinates are available in $p(:, k)$.

- *mesh.e* is the boundary element matrix, which contains information, such as nodal points for boundary elements and parameter values on the boundary elements, necessary to assemble the boundary conditions on $\partial\Omega$.

- *mesh.t* is the element matrix, containing information necessary to assemble our PDE on the domain, Ω. It contains information regarding the node points of the finite element mesh and the subdomain number of each element.

Optional fields:

- *mesh.v* is the vertex matrix. It contains the required information to recreate the geometry vertices.
- *mesh.equiv* is the equivalence matrix. This contains the information on equivalent boundary elements on equivalent boundaries.

Definitions for fields taken from [10].

4.4 Solver algorithms

In this section we discuss the three solvers that are available in our software to solve our sets of equations. Once our equations have been assembled into mass and stiffness matrices, we proceed to solve them using either a direct solver: Gaussian elimination, or one of the two iterative methods available: GMRES or conjugate gradients. This section gives the fundamentals of how the solver works.

4.4.1 Gaussian Elimination

We consider a linear algebraic system of m equations in n unknowns

$$a_{11}x_1 + a_{12}x_2 + ... + a_{1n}x_n = b_1$$

$$a_{21}x_1 + a_{22}x_2 + ... + a_{2n}x_n = b_2$$

$$\vdots \quad \vdots$$

$$a_{m1}x_1 + a_{m2}x_2 + ... + a_{mn}x_n = b_m$$

In matrix form this is $A\mathbf{x} = \mathbf{b}$, where $A = [a_{ij}]$ is a matrix of order $m \times n$ and $\mathbf{x} = [x_i]$ and $\mathbf{b} = [b_i]$ are n and m dimensional column vectors respectively, with $m \geq 2$. The a_{11} entry, is called the first pivot entry. If we denote the coefficients in the matrix by $a_{ij}^{(1)} = a_{ij}$ and the right hand side by $b_i^{(1)} = b_i$, we want to first solve the system $A^{(1)}\mathbf{x} = \mathbf{b}^{(1)}$. We solve this by elimination of columns. The elimination of the first column is carried out first. We eliminate the first variable from the remaining equations by multipling the first row by $-\frac{a_{i1}^{(1)}}{a_{11}^{(1)}}$. We then repeat this process for the second column, third column and so on until we get values for each of the unknowns.

4.4.2 GMRES

The GMRES method is a Krylov subspace method applicable to any non-singular matrix A. It is based on an orthogonality relation. The first step of the GMRES algorithm is to generate a set of basis vectors $v_1, ..., v_m$ of the m^{th} Krylov subspace, where m is user specified. The algorithm generates an $(m+1) \times m$ Hessenberg matrix

$$\hat{H_m} = \begin{pmatrix} (Av_1, v_1) & (Av_2, v_1) & (Av_3, v_1) & \dots & (Av_m, v_1) \\ (Av_1, v_2) & (Av_2, v_2) & (Av_3, v_2) & & (Av_m, v_2) \\ & (Av_2, v_3) & (Av_3, v_3) & & (Av_m, v_3) \\ & & (Av_3, v_4) & \ddots & \\ & & & \ddots & (Av_m, v_m) \\ & & & & (Av_m, v_{m+1}) \end{pmatrix}$$

and the orthonormal vectors v_i.

The pseudo-code for the GMRES algorithm is given in Algorithm 1. We note that $\beta = \|r_o\|_2$ and $\beta v_1 = r_0$.

Algorithm 1

1: Compute $r_0 = b - Ax_0$, $\beta = \|r_o\|_2$ and $v_1 = \frac{r_0}{\beta}$.

2: Define $\hat{H_m}$ and set elements h_{ij} to zero.

3: **for** $j = 1, 2, ..., m$ **do**

4: Compute $w_j = Av_j$

5: **for** $i = 1, ..., j$ **do**

6: $h_{ij} = (w_j, v_i)$

7: $w_j = w_j - h_{ij}v_i$

8: **end for**

9: $h_{j+1,j} = \|w_j\|_2$. **if** $h_{j+1,j} = 0$ set $m = j$ and **goto** 12

10: $v_{j+1} = w_j / h_{j+1,j}$

11: **end for**

12: Compute y_m as the minimiser of $\left\|\beta e_1 - \hat{H}_m y\right\|_2^2$ and set $x_m = x_0 + V_m y_m$.

Algorithm taken from [11].

4.4.3 Conjugate gradients

The GMRES algorithm is applicable to any non-singular system $Ax = b$. When the matrix A is strictly positive definite considerable computational savings can be achieved by using the Conjugate Gradient (CG) algorithm. The savings are a result of the Heissenberg matrix reducing to tridiagional form and allowing the orthonormal basis for the m^{th} Krylov subspace to be constructed by way of a three term recurrance relation known as the Lanczos algorithm.

The efficient implementation of the conjugate gradient algorithm is based on a variety of the orthogonality relation - (i) The residua, r_j, are orthogonal to each other, where the residua $r_m = b - Ax_m$, (ii) The search directions p_j are A-orthogonal ($(Ap_j, p_j) = 0$ for $i \neq j$). The pseudo-code for the CG algorithm is given in Algorithm 2.

Algorithm 2

1: Compute $r_0 = b - Ax_0$, $p_0 = r_0$

2: **for** $j = 0, 1, ...$ until convergence **do**

3: $\alpha_j = (r_j, r_j)/(Ap_j, p_j)$

4: $x_{j+1} = x_j + \alpha_j p_j$

5: $r_{j+1} = r_j - \alpha A p_j$

6: $\beta_j = (r_{j+1}, r_{j+1})/(r_j, r_j)$

7: $p_{j+1} = r_{j+1} + \beta_j p_j$

8: **end for**

Algorithm taken from [11].

4.5 Comparison of the solver techniques

In this section we briefly compare the three solvers discussed above for a standard problem that we will be investigating. For details on this problem see Chapter 4. We have plots for the time taken for the solution to converge and the number of iterations taken to reach the converged solution.

It can clearly be seen from the graphs that the conjugate gradient method converges to the solution in both the quickest time and with respect to the least number of iterations. The conjugate gradient method is followed closely by the GMRES algorithm, whereas the Direct method takes a considerable amount of time/iterations longer/more than the other two solvers - it almost takes three times longer to reach the converged solution than the GMRES solver for 6000 elements.

Having set an error tolerance on what would be deemed as an acceptable er-

ror in our solution, et, the direct method always seems to give a smaller error ($\leq et$) than the two iterative solvers. This can possibly be explained in that, given a solution that converges in n iterations, the direct method (taking more iterations to converge) at iteration $n-1$ is much closer to the accepted error tolerance then the two iterative schemes. Hence we *overshoot* the error tolerance by more. The same argument can be used to explain why the errpr is smaller for GMRES then for CG.

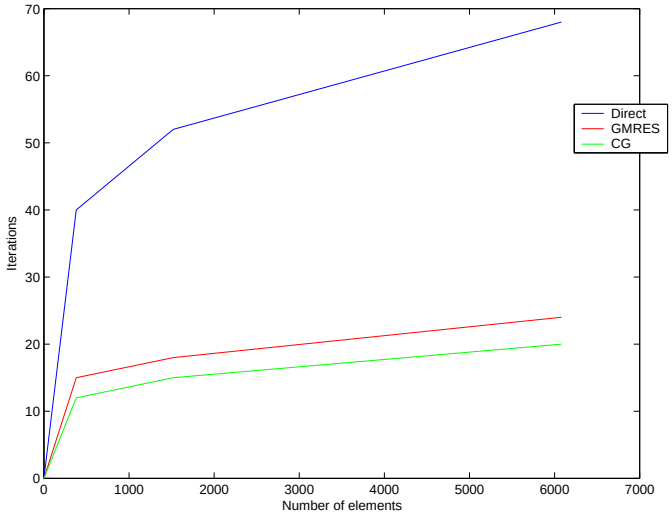

Figure 4.2: Comparison of iteration count for three solver algorithms

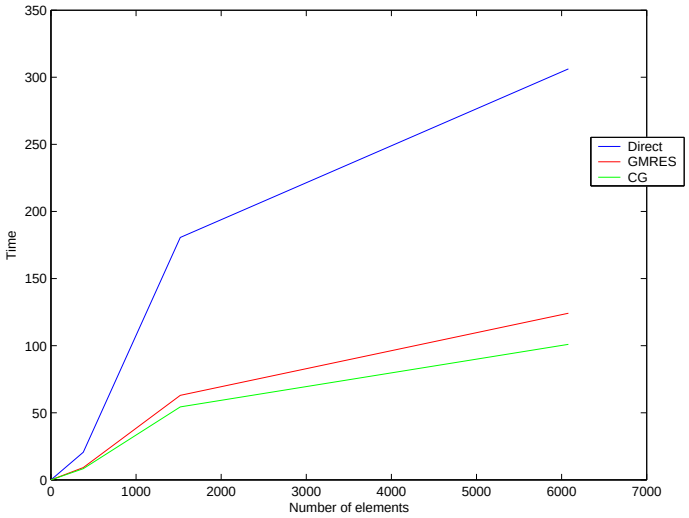

Figure 4.3: Comparison of time to solve problem for three solver algorithms

Having discussed the theory behind our viscoelastic flow problem and explored the techniques that can be employed to solve them, we move on to solving the actual problems. The general style of the subsequent chapters will be to present the results for the flow of viscoelastic flow on a standard length scale (10^0) first. We then proceed to solve the same problem on the scale of microns and see how the results differ. If they differ we will look into how they differ and try and discover trends in the patterns of change.

We will use a refined mesh of approximately 6000 elements in order to decrease the error in our solution. Increasing the number of elements will increase the acuuracy in our solution as we will be computing the value at a node, i, using surrounding nodes that are much closer to the node i. We will set an error tolerance of $et = 10^{-12}$. This means that a solution will be considered to have converged if the error in the solution is less than et. The itertion which takes the solution over this value will be the last iteration and the iterative process

will terminate and we will have our solution.

The problem is set-up in Femlab by first drawing the geometry and defining relevant constants. The equations are then entered for the domain and the boundary conditions are set. The mesh is then initilized and refined to produce the required number of elements and the problem is solved.

We explore three specific geometries. Chapter 4 looks at the case of two parellel plates, both stationary (Figure 3.4), Chapter 5 looks at two parellel plates, the upper plate moving with constant velocity (Figure 3.5) and Chapter 6 looks at two parellel plates that are being compressed togeher from forces on the top and bottom (Figure 3.6).

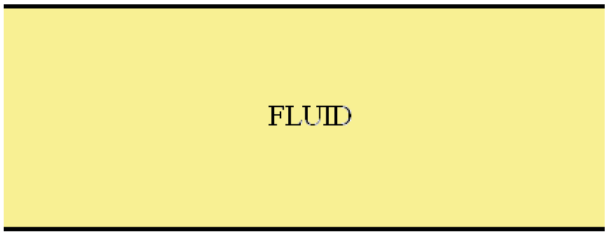

Figure 4.4: Two parellel plates

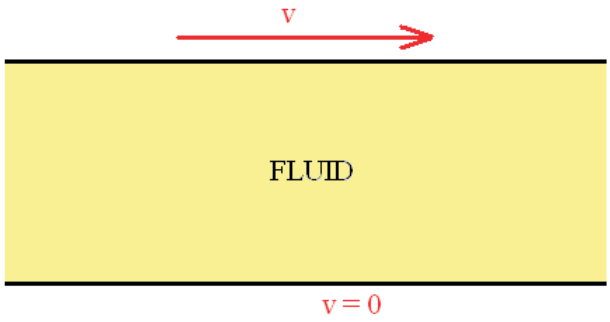

Figure 4.5: Two parellel plates with the top plate moving with velocity, v

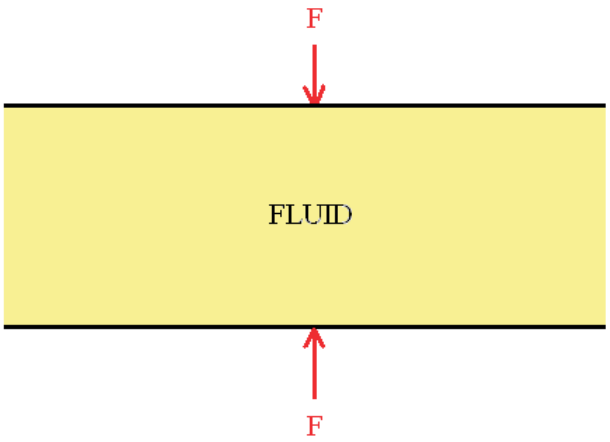

Figure 4.6: Two parellel plates under compressive forces

Chapter 5

Modelling viscoelastic flow between two parellel plates

5.1 The problem

We consider an Oldroyd-B model of viscoelastic flow, with constitutive equation as given in (1.33). We proceed to solve this equation coupled with the equation for continuity and the equaton of motion for a geometry comprising of two parellel plates with $-1 \leq x \leq 1$ and $-0.2 \leq y \leq 0.2$ - effectively a rectangle with the two ends open. With reference to Figure (4.1), the boundary labelled (1) will have an inflow boundary condition, with which we specify an inflow, *uin*. Across boundary (4) we will impose an outflow condition with the pressure at this boundary initially equal to 0. On the remaining boundaries, (2) and (3), we will impose the no-slip boundary condition. To start our model off, we use an initial model of Newtonian flow, and then proceed to solve for non-Newtonian flow - the Newtonian flow acts effectively as our initial condition. On obtaining our solution for our standard length scale ($l = 10^0$) we will perform the same process on a smaller scaled model of the problem and compare and contrast the

results.

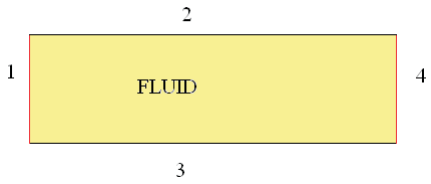

Figure 5.1: Boundaries of our domain

5.2 Results

On solving for the scenerio dictated above, we present first the graphical results and then discuss them.

5.2.1 Graphical results

Velocity profiles

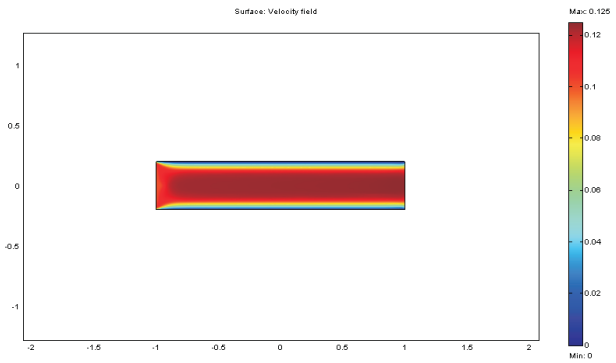

Figure 5.2: Velocity profile for our standard length scale, $l = 10^0$

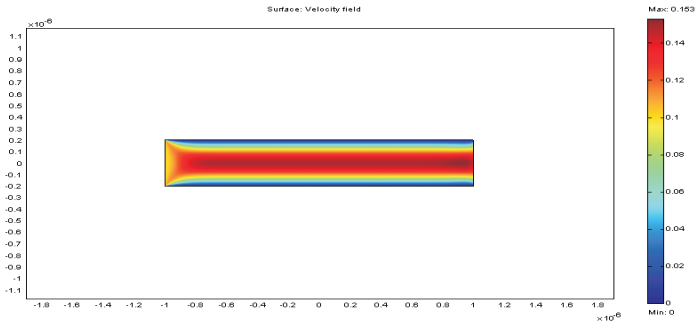

Figure 5.3: Velocity profile for length scale $l = 10^{-6}$

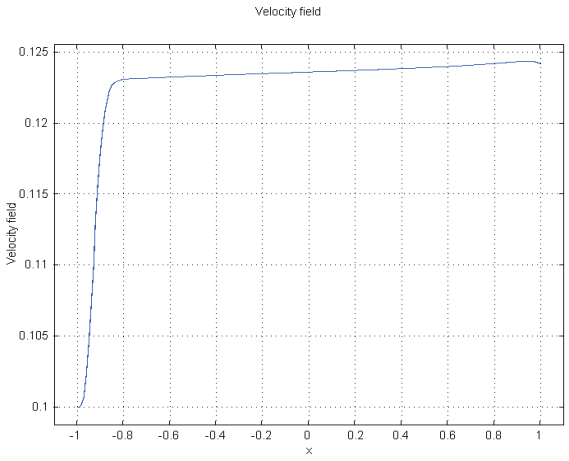

Figure 5.4: Velocity profile for cross-section $y = 0$ - length scale $l = 10^{0}$

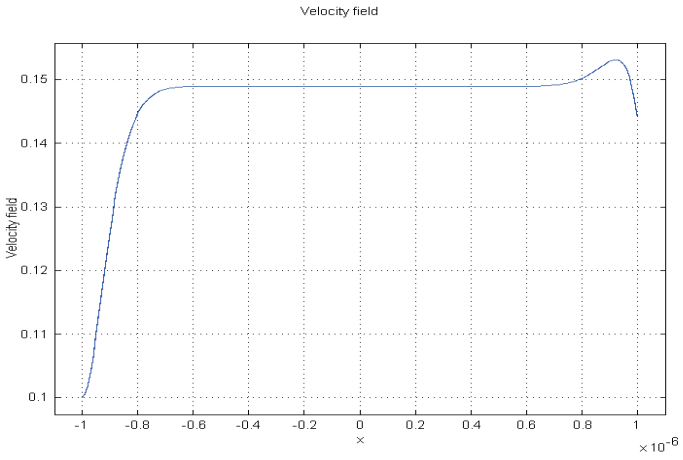

Figure 5.5: Velocity profile for cross-section $y = 0$ - length scale $l = 10^{-6}$

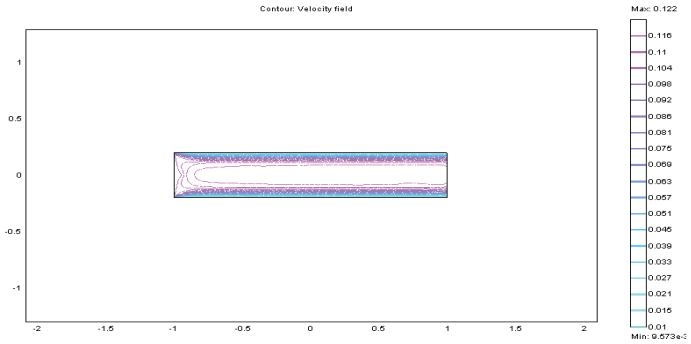

Figure 5.6: Velocity Contour plot for $l = 10^0$

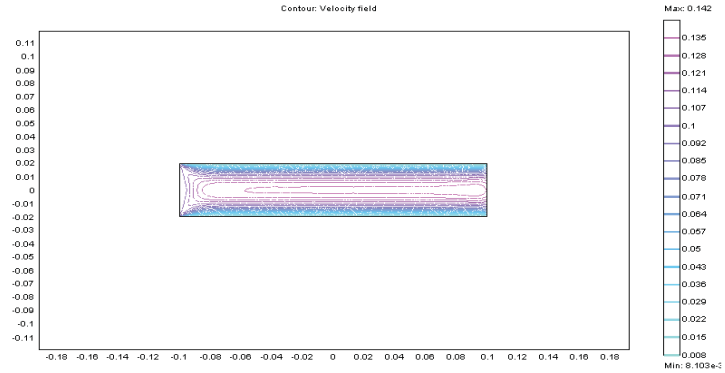

Figure 5.7: Velocity Contour plot for $l = 10^{-1}$

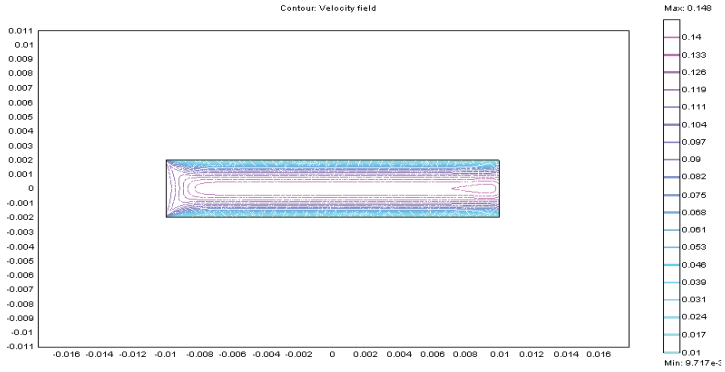

Figure 5.8: Velocity Contour plot for $l = 10^{-2}$

Pressure profiles

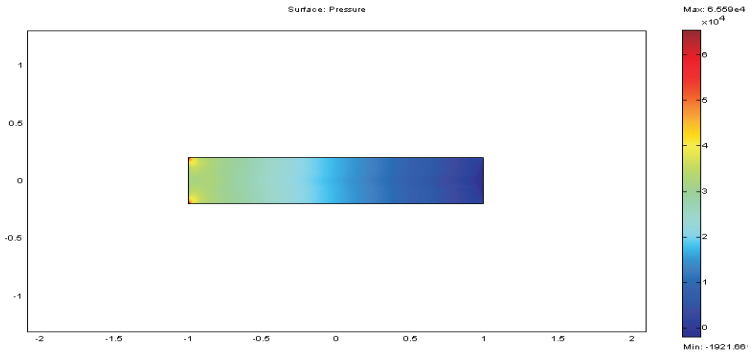

Figure 5.9: Pressure profile for $l = 10^0$

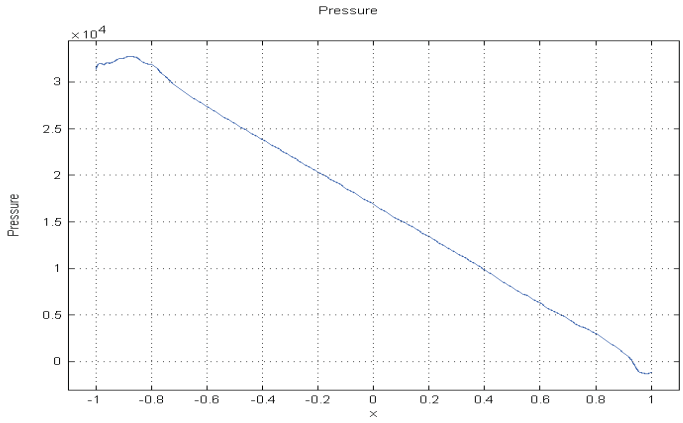

Figure 5.10: Pressure profile for cross section $y = 0$ for $l = 10^0$

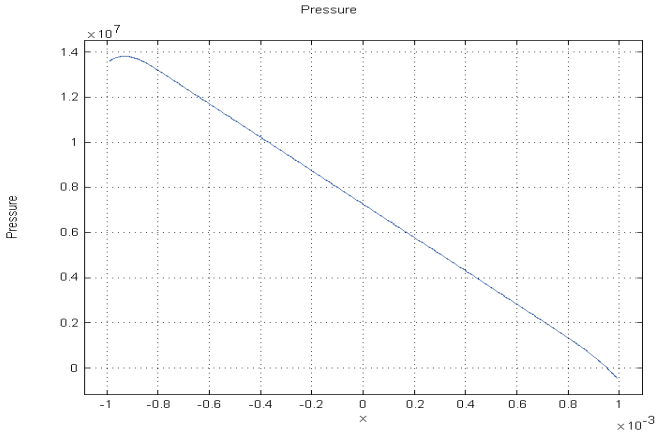

Figure 5.11: Pressure profile for cross section $y = 0$ for $l = 10^{-3}$

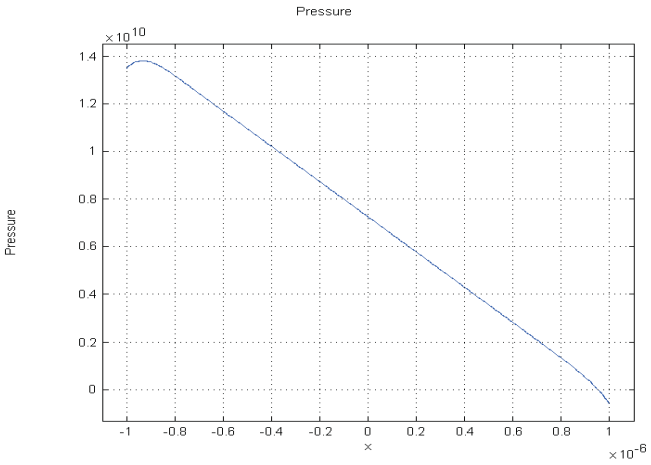

Figure 5.12: Pressure profile for cross section $y = 0$ for $l = 10^{-6}$

Vorticity profiles

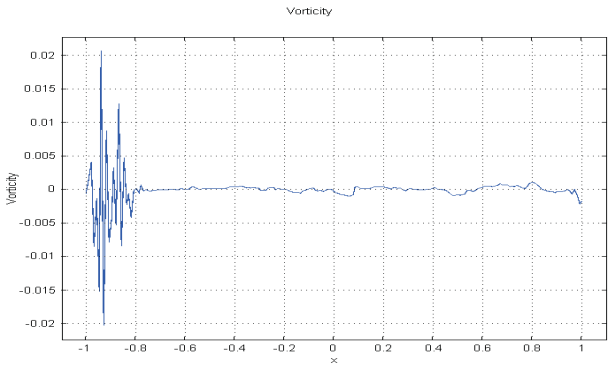

Figure 5.13: Vorticity profile for $l = 10^0$-cross section y=0

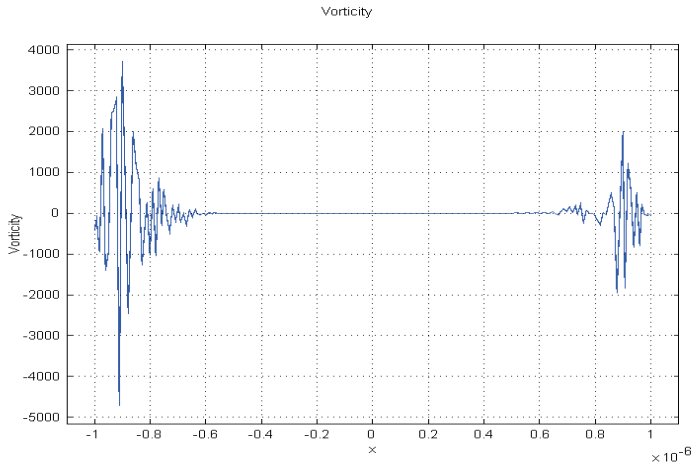

Figure 5.14: Vorticity profile for $l = 10^{-6}$ - cross section y=0

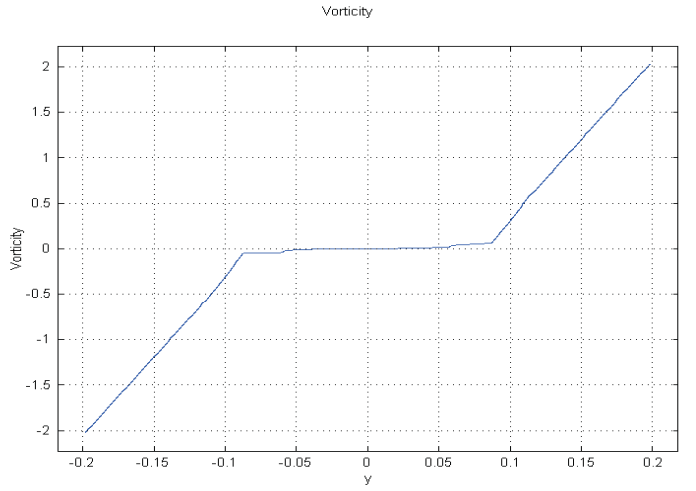

Figure 5.15: Vorticity profile for $l = 10^{0}$ - cross section x=0

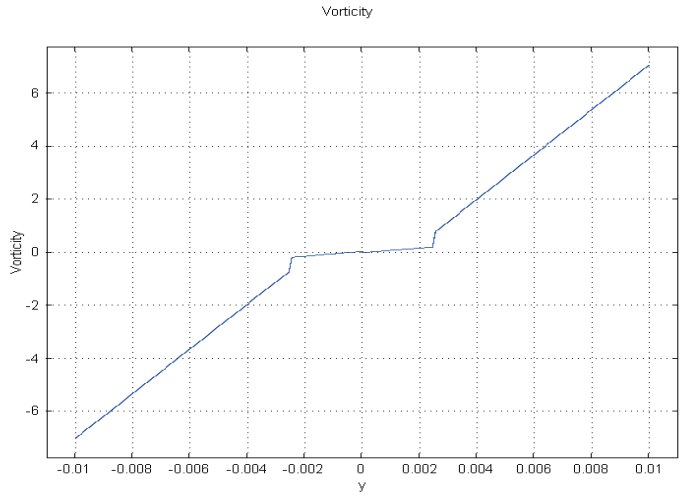

Figure 5.16: Vorticity profile for $l = 10^{-1}$ - cross section x=0

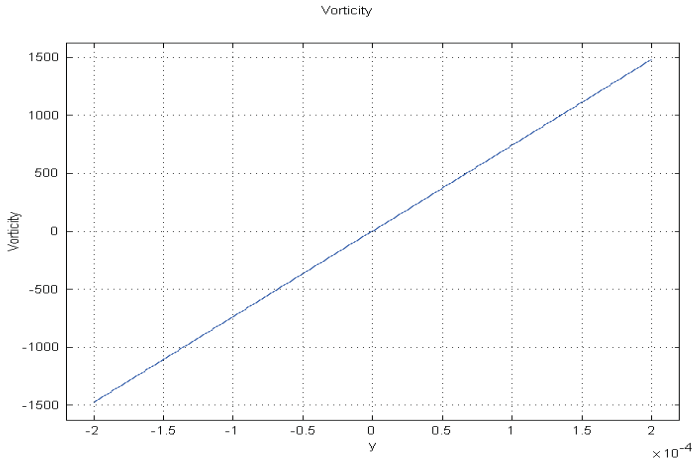

Figure 5.17: Vorticity profile for $l = 10^{-3}$ - cross section x=0

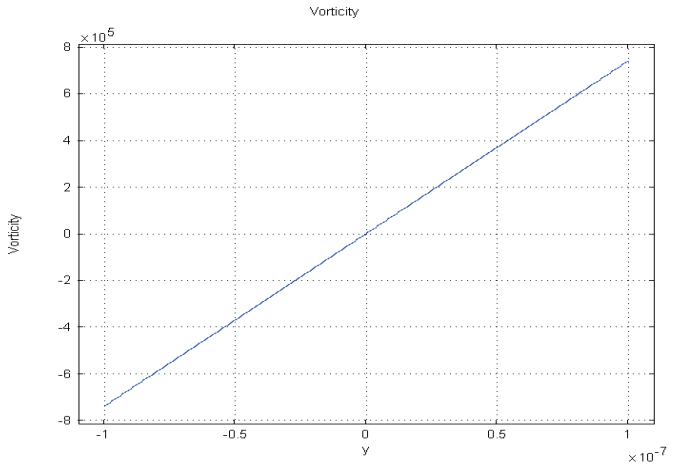

Figure 5.18: Vorticity profile for $l = 10^{-6}$ - cross section x=0

5.2.2 Discussion of results

As can be seen from the 2D velocity profiles, the velocity between the two plates looks, at first glances, very similar. On detailed inspection it can be observed that the velocities for the standard problem, $l = 10^0$, are lower than that for the micron length problem, given the same inflow velocity at boundary 1. Investigation into lengths scales between these two extremes shows that in fact the velocity does increase each time we decrease the length scale.

In each case of differing lengths, the problem is symmetric about the $y = 0$ axis, and the flow patterns, when looking at cross sections parellel to the y-axis, is the same shape for each of the length scales. The only difference is the maximum velocity being higher in each subsequent length scale between $l = 10^0$ and $l = 10^{-6}$, where the length scale decreases each time by a factor of 0.1.

Turning our attention to the horizontal cross sections (parellel to the x-axis) we do have a significant difference as the length is decreased. With reference

to Figure 4.4, we notice the curve for the velocity increases dramatically between $x = -1$ and $x \approx -0.8$ before continuing to increase but at a much slower rate (acceleration $\approx 2.77 \times 10^{-3} units second^{-2}$). At boundary 4 we have the flow leaving with velocity $\approx 0.125 units second^{-1}$. In the case of the length scale $l = 10^{-6}$, Figure 4.5, we have the same dramatic increase in velocity between $x = -1 \times 10^{-6}$ and $x \approx -0.8 \times 10^{-6}$, with the velocity increasing to $0.15 units second^{-1}$. The velocity then remains approximately constant up until $x = 0.8$, where we have a sudden increase (peak) and then decrease to a velocity lower than it was prior to the peak (velocity $\approx 0.145 units second^{-1}$). This is a significant difference compared to the standard case, and warrants further investigation. Proceeding to investigate lengths between the two already investigated, we find that this occurance does occur in all of the other length scales, becoming more and more apparent as the length is decreased - (it starts as a mild raise in the velocity at $x \approx 0.8$ and becomes more and more of a peak as the length is reduced). It should also be noted that the peak begins to rise at latter x values as the length is decreased. The difference between the point at which the peak begins at subsequent lengths is not hugely different, but is certainly noticably. This occurance can be seen more clearly from the contour plots of the velocity - there is an aerofoil style shape towards the end of the flow pattern, symmetric and centred at $y = 0$, which gets smaller and smaller as the length scale is decreased - evident in Figures 4.6, 4.7, 4.8. This latest observation also begs the question as to whether the standard length scale also has a peak, but perhaps it starts very early and instead of resembling a peak as such, it is more of a gentle rise and a drop-off at the end. From the graphical output the existence of a peak isn't obvious, however there is a small dip in the velocity at the end (at $x \approx 1$), which may be a strong indication of a peak. If this is the case the peak would be very long horizontally and its height would be considerably small.

In order to draw some sort of understanding as to whether this occurance would

continue as the length scale approaches the nano or pico scales, the flow patterns were calculated for the length scale $l = 10^{-12}$. The pattern achieved for this model was as expected from making the hypothesis that the peak would increase in size and the maximum velocity reached would increase as well. It is, therefore, a safe bet to assume that this would continue as the length scale is reduced more and more, under the assumption that our model decribes the flow adequetely.

We next turn our attention to the pressure profiles of our solutions. In all cases investigated, when looking at the 2D pressure profiles, the pressure is greatest at the inflow boundary and least at the outflow boundary. More specifically, the pressure is greatest at the corners of the plates at the inflow boundary. The pressure increases as the length scale is reduced more and more, as would be expected from the velocity results. The pressure profile is symmetric about the $y = 0$ axis, again consistent with our velocity profiles. We now look at the cross section across $y = 0$. For our standard length scale the pressure starts off high before decreasing steadily towards its minimum value (Figure 4.10). It tails off at the $x \approx 0.9$ with almost a '*flick*'. Towards the inflow boundary the pressure fluctuates slightly, before steading out at $x \approx -0.7$. The cross section profiles, as we reduce the length scale, all start at a higher pressure and have a small rise before steadily decreasing towards 0. The small '*flick*' evident in our standard length scale is no longer apparent, replaced instead by a smooth curve (Figures 4.11 and 4.12). As we continue to reduce the length the pattern is still the same, the only difference being the initial pressure at the inflow boundary being greater each time.

Our final discussion with regards to the behaviour of the flow for this geometry is with regards to the vorticity. First we look at cross sections parellel to the y-axis. For our standard length scale this looks likes three ramps, the

first and third with steep gradients(≈ 17.5) and the second with almost a flat slope(gradient ≈ 1.25) (Figure 4.15). The ramps cover the following regions respectively: [-0.2,-0.08], [-0.08,0.08], [0.08,0.2]. If we decrease the length scale by a factor of 10, we get a similar graph, but with a wall at the end of the first slope and at the beginning of the third. The vorticity also has lower value on the lower y boundary and a higher value on the upper y boundary, compared to the standard length scale (Figure 4.16). Further reductions in the length scale sees the three slopes replaced by a continuous straight line, and the vorticity decreasing more and more on the lower y boundary and increasing more and more on the upper y boundary (Figure 4.17 and 4.18). This pattern continues as we reduce the length scale towards $l = 10^{-12}$, so it is a safe assumption that for small scale flows the vorticity across sections of the flow parellel to the y-axis will behave in this way.

Now considering cross-sections parellel to the x-axis, we get interesting behaviour. As demonstrated in Figures 4.13 and 4.14 the vorticity behaves in a fluctuating, random manner as we move along the x-axis. Investigating all the length scales a factor of 10 different between $l = 10^0$ and $l = 10^{-6}$, we see that the vorticity remains roughly equal to 0 between -0.6 and 0.8, with slight fluctuations here and there. On the other side of these two boundaries, the vorticity behaves in what can best be described as a chaotic manner. No fixed pattern can be seen as we reduce the length scale, so unfortunately we cannot make any predictions about the vorticity of the flow parellel to the x-axis.

This concludes our discussion on our first geometry. Conclusions for this geometry will be discussed in the conclusion, where we can discuss the three geometries together. We now move onto our second geometry - two parellel plates, with the top plate moving.

Chapter 6

Modelling viscoelastic flow between two parellel plates, the upper plate moving

6.1 Theory and equations

We continue to consider an Oldroyd-B model for the flow of our viscoelastic fluid. Our domain in this chapter comprises of the same setup as with the parellel plates in the previous chapter with the exception that we consider a fluid enclosed in this area (i.e. no inflow) and we move the upper parellel plate with a given velocity. With regards to our diagram of the setup, given in Figure 5.1, we will impose no slip conditions on boundaries (1) and (3), an outflow condition on boundary (4) and a inflow condition on boundary (2), with the velocity being purely horizontal, to act as if a plate is moving at this boundary. Our processes and analysis of results will be the same as in the previous chapter.

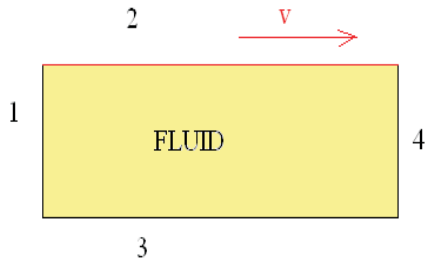

Figure 6.1: Boundaries of our domain

6.2 Results

Upon solving our problem as described above, we present first the graphical results before proceeding to a discussion on their meanings.

6.2.1 Graphical results

Velocity profiles

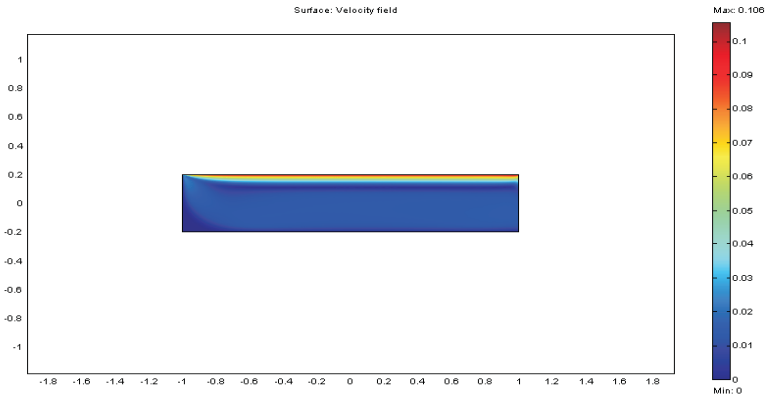

Figure 6.2: Velocity profile $l = 10^0$

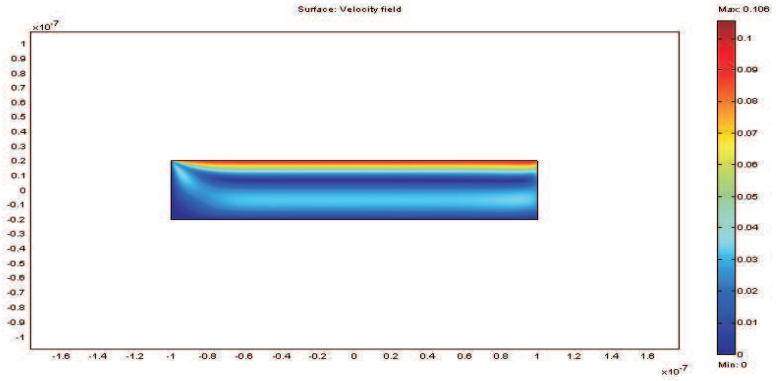

Figure 6.3: Velocity profile $l = 10^{-6}$

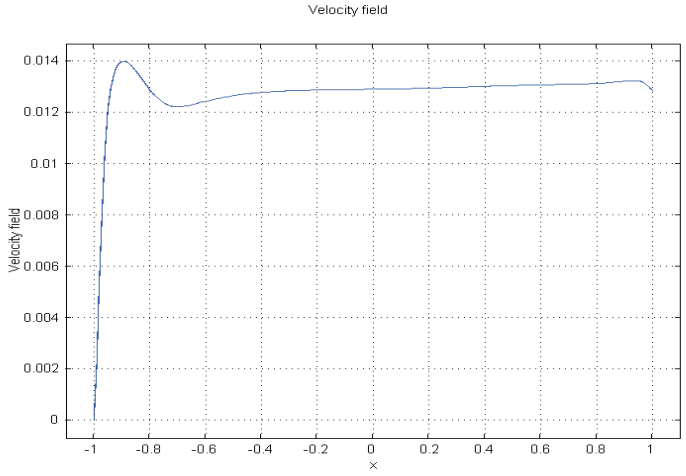

Figure 6.4: Velocity cross section, $y = 0$, $l = 10^{0}$

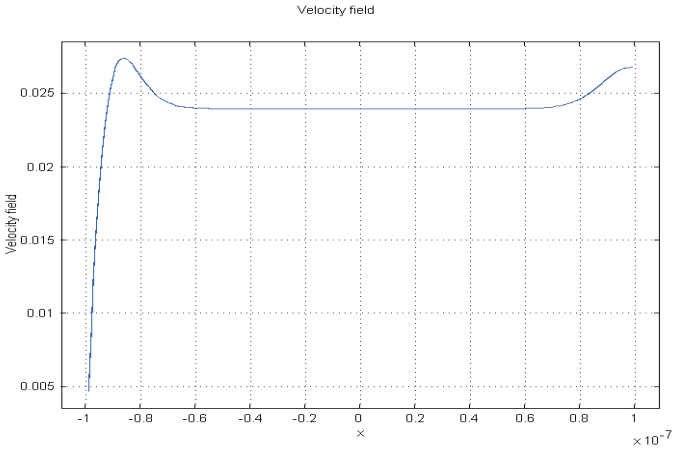

Figure 6.5: Velocity cross section, $y = 0$, $l = 10^{-6}$

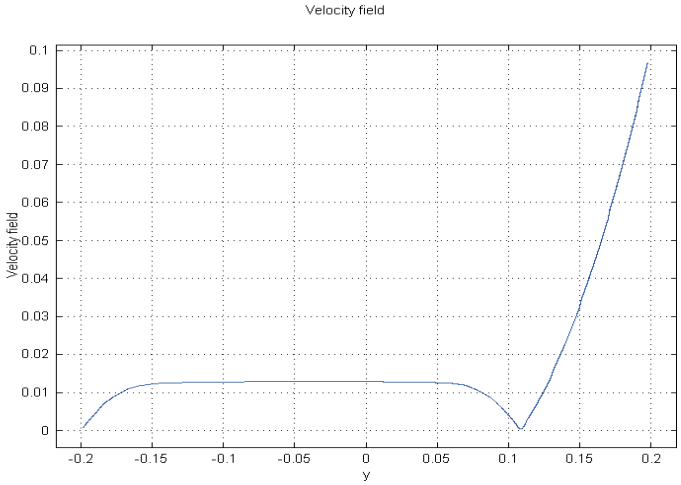

Figure 6.6: Velocity cross-section, $x = 0$, $l = 10^{0}$

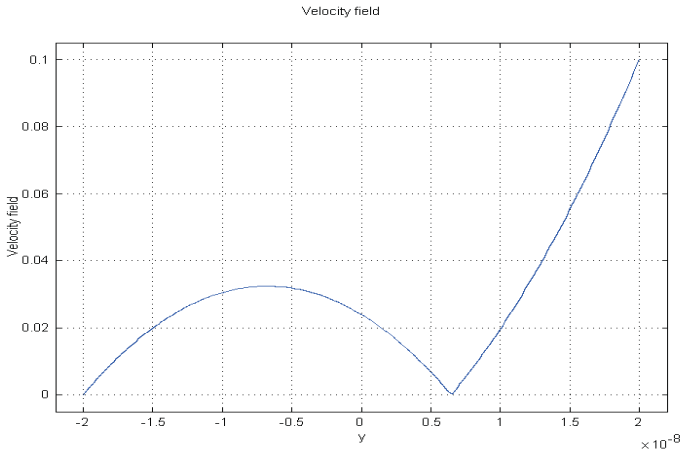

Figure 6.7: Velocity cross section, $x = 0$, $l = 10^{-6}$

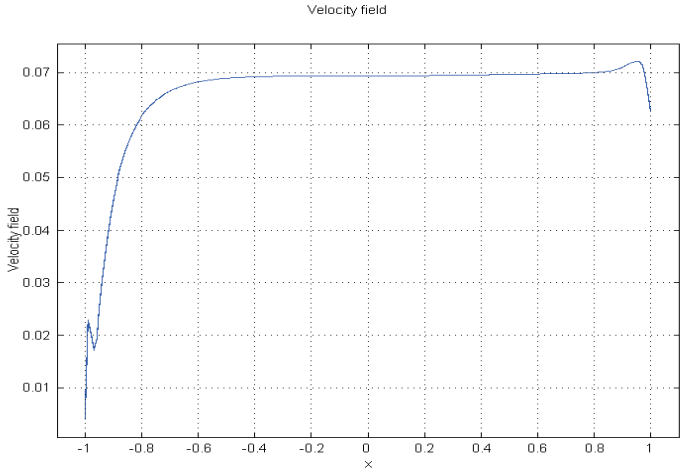

Figure 6.8: Velocity cross section, $y = 0.18$, $l = 10^{0}$

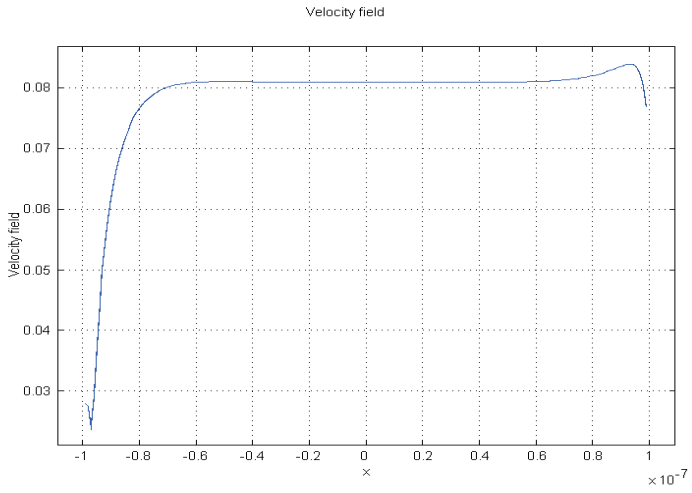

Figure 6.9: Velocity cross section, $y = 0.00000018$, $l = 10^{-6}$

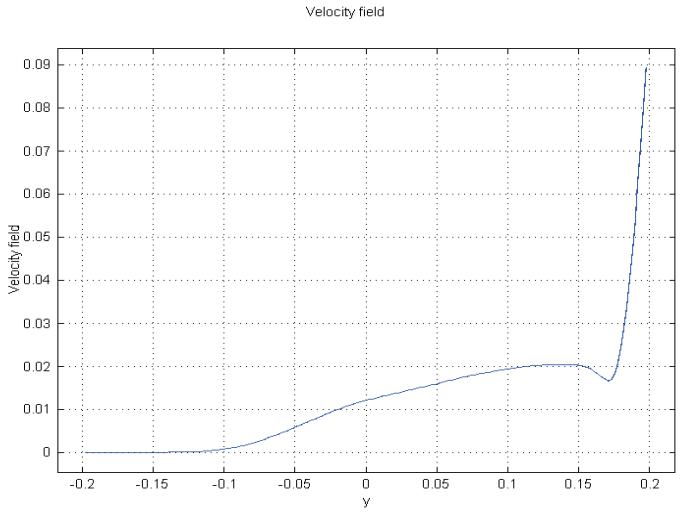

Figure 6.10: Velocity cross section, $x = -0.95$, $l = 10^{0}$

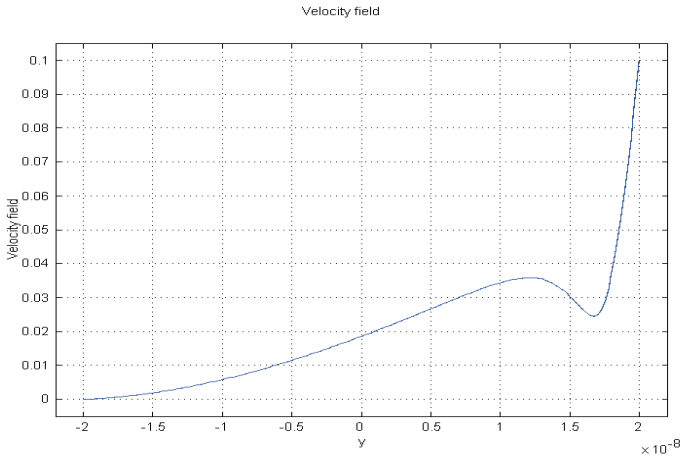

Figure 6.11: Velocity cross section, $x = -0.000000095$, $l = 10^{-6}$

Pressure Profiles

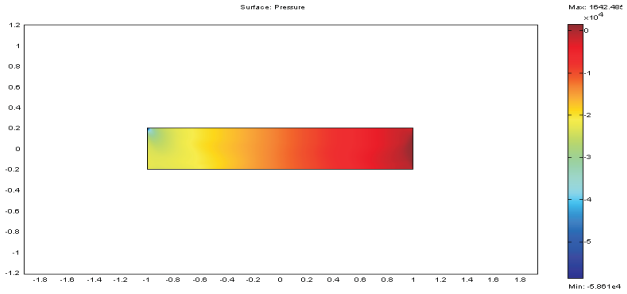

Figure 6.12: Pressure profile for $l = 10^0$

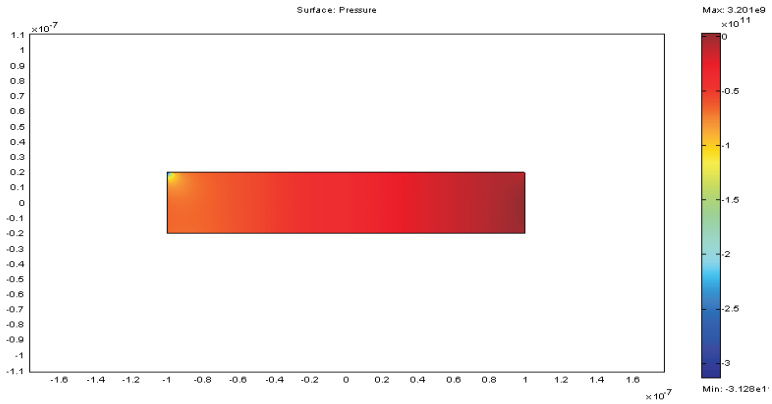

Figure 6.13: Pressure profile for $l = 10^{-6}$

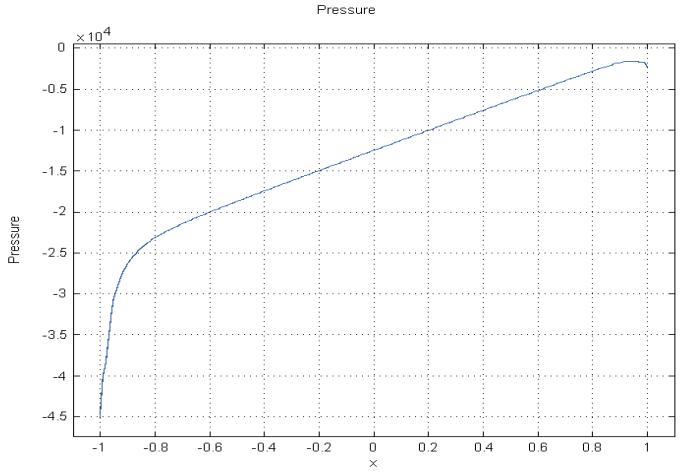

Figure 6.14: Pressure cross section profile for $l = 10^{0}$, y=0.18

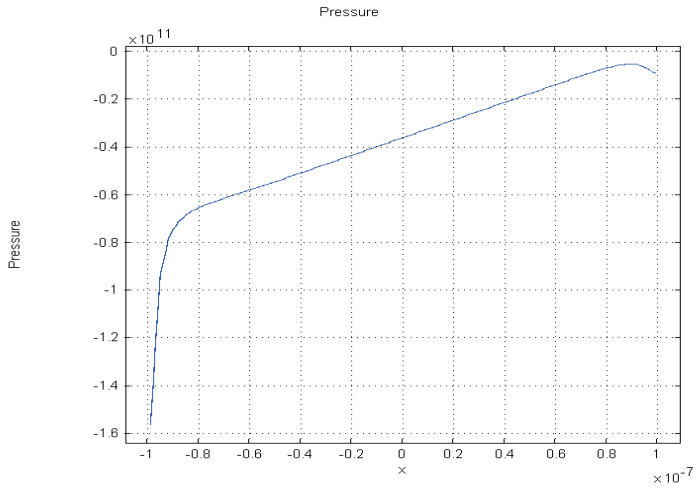

Figure 6.15: Pressure cross section profile for $l = 10^{-6}$, $y = 0.000000018$

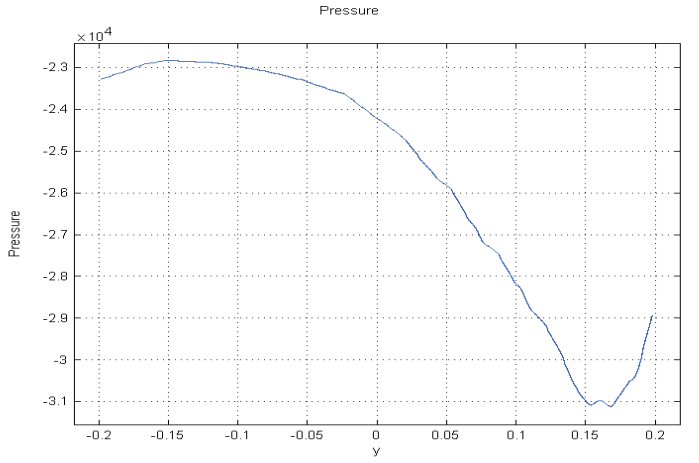

Figure 6.16: Pressure cross section profile for $l = 10^{0}$, $x = -0.95$

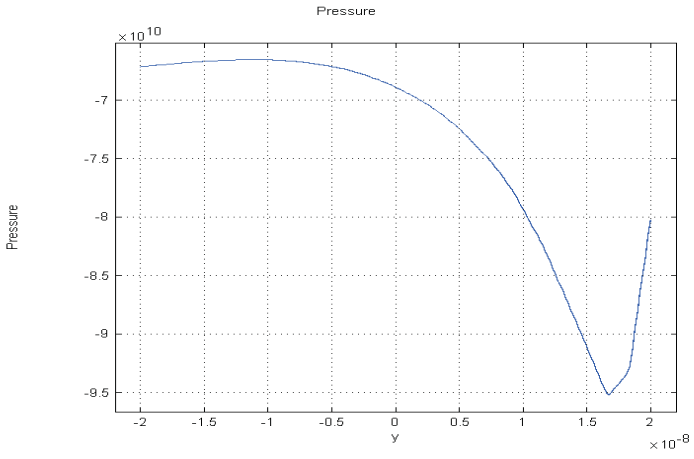

Figure 6.17: Pressure cross section profile for $l = 10^0$, $x = -0.000000095$

Vorticity Profiles

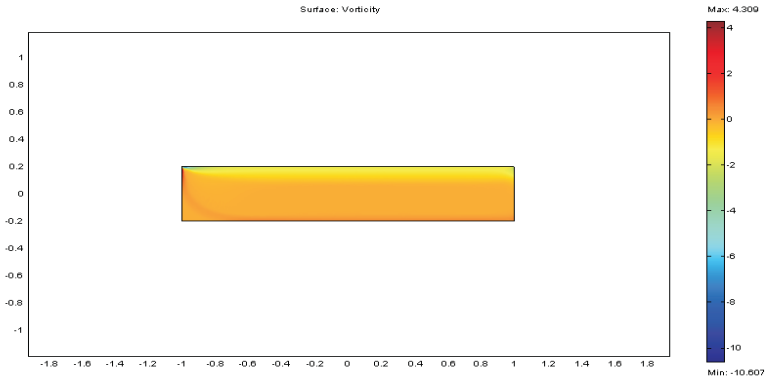

Figure 6.18: Vorticity profile $l = 10^0$

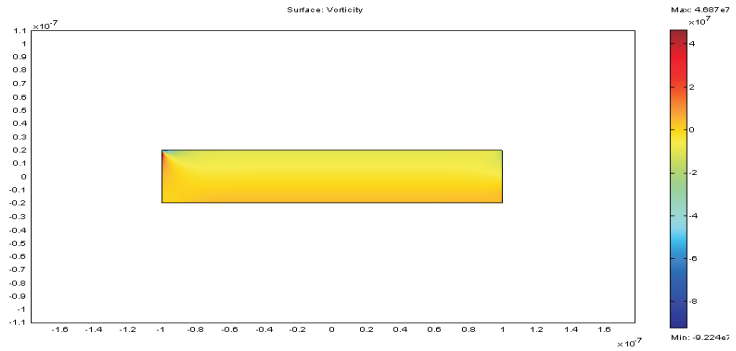

Figure 6.19: Vorticity profile $l = 10^{-6}$

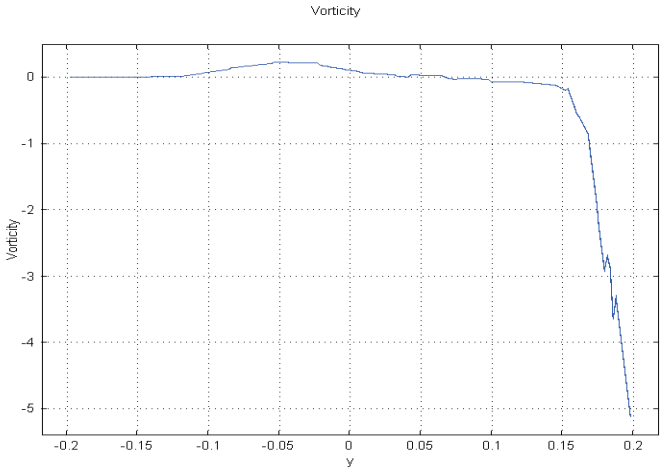

Figure 6.20: Vorticity cross section, $x = 0.95$, $l = 10^{-6}$

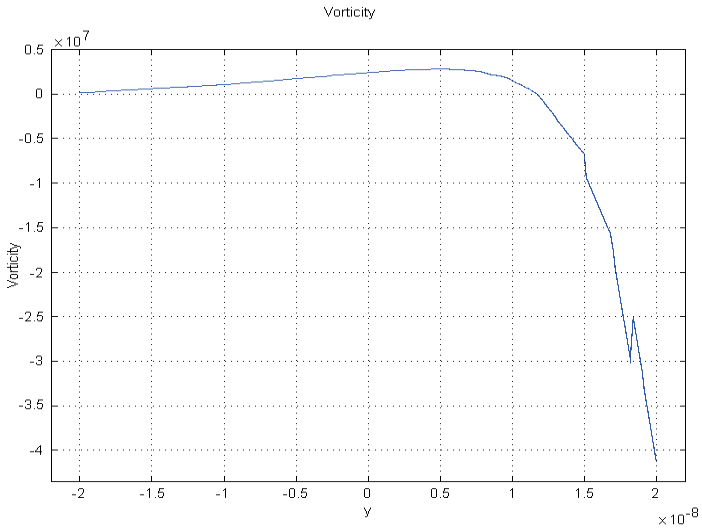

Figure 6.21: Vorticity cross section, $x = -0.000000095$, $l = 10^{-6}$

6.2.2 Discussion of Results

We first look at the velocity profiles for our models. In both the standard and micron length scales we can observe that the velocity is highest on the boundary where the parellel plate is moving with a velocity and least on the stationary boundary. This is as would be expected. There is evidence of what is known as *clogging* in the lower left hand corner of the models for all the length scales ranging from $l = 10^0$ and $l = 10^{-6}$. This can be observed as the velocity of the fluid in this region of the domain is zero (Figure 5.2 and 5.3). From Figure 5.3 it is visible that there is also a significant area of *clogging* just above the $y = 0$ line, which does not occur in such a large amount in the standard length scale case. Investigation into lengths between $l = 10^0$ and $l = 10^{-6}$ show that this area slowly grows in size - so this would be an effect relating to the reduction of length scale. The clogging at this point also has the knock on effect of the velocities surrounding it, particularly on the underside, being smaller then for the $l = 10^0$ model. This again is proved to be correct by investigation into the lengths between our two extremes, where there is evidence of the velocities around the clog getting smaller and smaller with the reduction of length.

In Figures 5.4 and 5.5 we have cross sections of the velocity profiles across $y = 0$. The two profiles look very similar, with the $l = 10^{-6}$ profile almost being a scaling of the $l = 10^0$ profile by ≈ 1.5. The only major difference occurs at the right hand side of the plots, where on our $l = 10^{-6}$ profile the graph curves upward, compared to our $l = 10^0$ profile, where the graph curves very slightly down. Looking at length scales between these two extremes we find that the *tail* of the graph does flatten out and then begin to curve upward. This implies that as the length scale is reduced, the exit velocity increases. Further investigation down to $l = 10^{-12}$ shows this to be true. It is also evident from these plots that as the length scale is decreased, the velocity across the cross section

increases compared to the previous length. However the rate at which the velocity increases slows down as we decrease the length scale, with the difference between the maximum velocity for $l = 10^0$ and $l = 10^{-1}$ being ≈ 0.011 and for $l = 10^{-5}$ and $l = 10^{-6}$ being ≈ 0.003. This suggests that further reduction of the length towards the nano/pico scales would result in a maximum velocity that is approximately the same.

Turning our attention to the cross section across $x = 0$, Figures 5.6 and 5.7, we see that as the length is reduced the parabola-like curve between $y = -0.2$ and $y \approx 0.1$ resembles an inverted x^2 curve and the length of the y-axis across which this parabola streches decreases. This has the effect that the remainder of the graph (which is a slightly curved line with gradient ≈ 0.45) has a smaller gradient than for the larger length scale. Further investigations again show that this is a continuing occurance between the two length extremes, with the parabola resembling an inverted x^2 curve more and more as the length scale is reduced and the length of the y-axis that the parabola exists on decreasing with length.

When looking at the velocity and indeed the vorticity and presure profiles, which we will discuss shortly, the area that begs to be investigated the most is the upper part of the profile, near the moving plate, and the top left hand corner. Concerning ourselves first with the former, we get Figures 5.8 and 5.9. The graphs are nearly identical but for the graph for $l = 10^{-6}$ having a higher maximum velocity and having a higher velocity at all points compared with the $l = 10^0$ model, and for the small sharp decrease and rise in velocity at $x \approx -0.95$. The former point fits in with what we have discussed previously - that the micron length scale has higher velocities than the standard length scale. The latter difference though is interesting. It can be noted from the two figures that the sharp decrease and increase in velocity occurs closer to the left boundary at $x = 1^{-6}$. Looking at the cross section for other length scale models

between $l = 10^0$ and $l = 10^{-6}$ shows that the sharp decrease and increase does move towards the left hand boundary more and more as the length is decreased, apart from at $l = 10^{-1}$ where it increases. Now if we look at the cross-section across $x = -0.95$ and $x = -0.00000095$ for our two length scales we get graphs that are almost identical, with an initial gentle rise in velocity, before a small dip occuring towards the top moving boundary followed by a sharp increase. The only major difference between the two graphs is that for $l = 10^{-6}$ the corresponding points when compared to the $l = 10^0$ graph are all slightly higher (accounted for with the velocity at the same points being higher for the smaller model). Having taken two cross sections that both involve the upper left hand corner of our domain, we see that it turns out that both our sharp drop and rise in velocities, evident in Figures 5.8 and 5.9, and the drop in velocity evident in Figures 5.10 and 5.11 both occur in this area. As they both involve decreases in and then increases in the velocity it can be suggested that perhaps we have a decrease in velocity in a pocket of the corner of the domain. Taking further cross sections, horizontally and vertically in this vicinity, and with reference to contour plots of the velocity, there is a small region with a lower velocity than the surroudings in this area, which moves closer to the left hand boundary ((1) in Figure 5.1) as the length is decreased. Looking at models for the flow in length scales between our two extremes confirms that this is indeed occuring.

We now turn our attention to the pressure profiles. Figures 5.12 and 5.13 show the pressure for the length scale $l = 10^{-6}$ is higher at equivalent points than for the length scale $l = 10^0$. This is to be expected as the velocity is greater for the smaller length scale, hence an increase in pressure. Taking cross section profiles across $x = 0$ and $y = 0$ shows that the pressure behaves in a similar way in both cases. Again, an area that warrants further investigation is the top left hand corner of the domain. Figures 5.14 and 5.15 show horizontal cross sections through this area. As can be seen they do not vary at all apart from

the length $l = 10^{-6}$ having higher values of pressure at each point compared to $l = 10^{0}$. Figures 5.16 and 5.17 show vertical cross sections through this area. These unlike the horizontal cross sections are different. For the length scale $l = 10^{0}$ the plot fluctuates whilst decreasing and at its minimum it has two troughs (towards the moving plate) before the pressure rises up again. For the other length scale, the plot is some what smoother and has one minimum, at approximately the same place as the second minimum for the previous plot. Analysis of what happens between these two length scales shows us that the curve flucutuates before smoothing out as the length is decreased, and the two minimums slowly join to form one (the small raise between the two minimums in Figure 5.16 gets smaller before joining to make one minimum at the length $l = 10^{-4}$). Relating this occurance to that mentioned at the end of the velocity profiles discussion, the drop in the pressure at this point corresponds to where our region of smaller velocity is.

Our final discusion for this scenario involves the vorticity. Figures 5.18 and 5.19 show the vorticity profile for the length scales $l = 10^{0}$ and $l = 10^{-6}$ respectively. Observing these and looking at cross sections across the $x = 0$ and $y = 0$ axis we see that the vorticity for both length scales is very similar, with the vorticity having a slightly higher magnitude for the $l = 10^{-6}$ case. As with the pressure, an area that looks of particular interest is the top left hand corner. Following the same method of taking vertical and horizontal cross sections we find that the horizontal cross sections are the same but the vertical cross sections, like with the pressure, are different, Figures 5.20 and 5.21. We can see two sharp increases followed by decreases in the vorticity profile for $l = 10^{0}$ compared to only one for $l = 10^{-6}$. As we have seen a similar situation before involving two troughs becoming one previously, it is a fair assumption that this is what occurs here. Looking at lengths scales between our two extremes, shows this assumption to be correct, again the two sharp increases and decreases become

one at the length scale $l = 10^{-4}$. Between the lenghts $l = 10^{0}$ and $l = 10^{-3}$ the two move closer together. It should also be noted that the solitrary *spike* on the vorticity profiles for lengths less than $l = 10^{-3}$ is larger than the two *spikes*. It is almost as if it is a combination of the two.

Chapter 7

Modelling viscoelastic flow between two compressive, parellel plates

7.1 Theory and equations

For our final geometry, we look at two parellel plates that are subjected to forces that make them come together - in effect what happens to the fluid when two plates are squeezed together. We make use of the same model of flow for our viscoelastic fluid, and our geometry that we use is two parellel plates with an initial stationary fluid between them. We will allow for outflow through both boundaries (1) and (4) and the parellel plates will move down and up respectively on boundaries (2) and (3) with a velocity given by -v and v, again respectively. All other aspects of our model remain as they have been for the other two geometries.

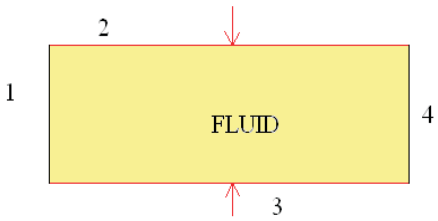

Figure 7.1: Boundaries of our domain

7.2 Results

7.2.1 Graphical results

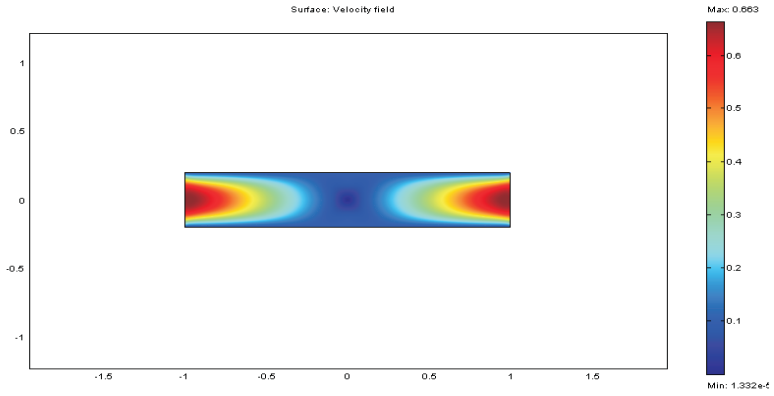

Figure 7.2: Velocity profile - $l = 10^0$

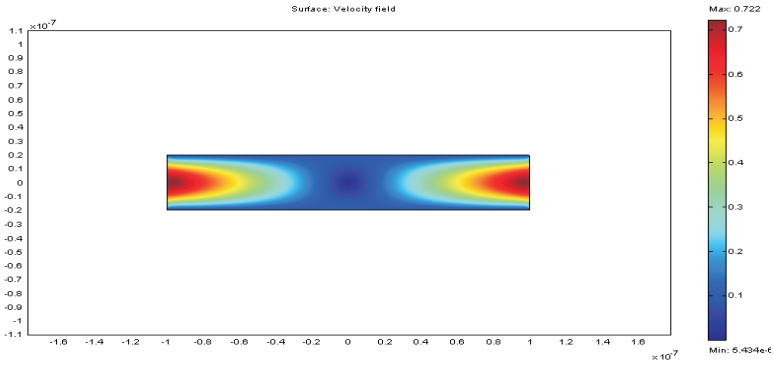

Figure 7.3: Velocity profile - $l = 10^{-6}$

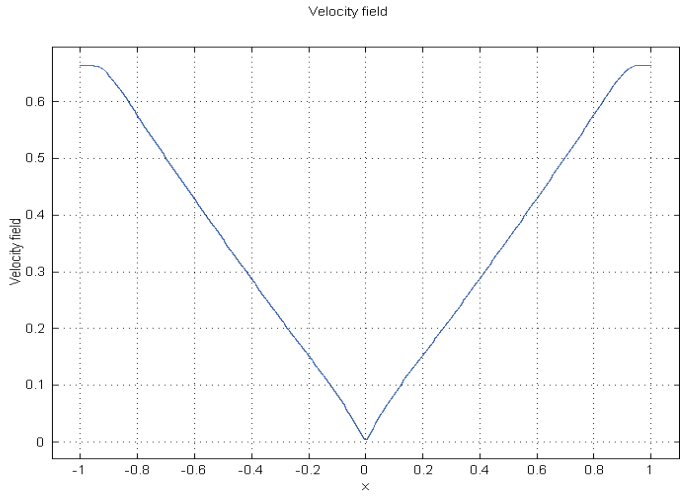

Figure 7.4: Velocity cross section, $y = 0$ - $l = 10^{0}$

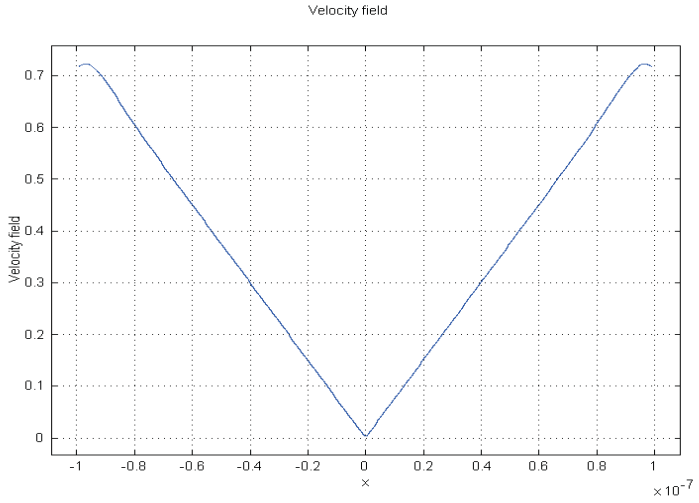

Figure 7.5: Velocity cross section, $y = 0$ - $l = 10^{-6}$

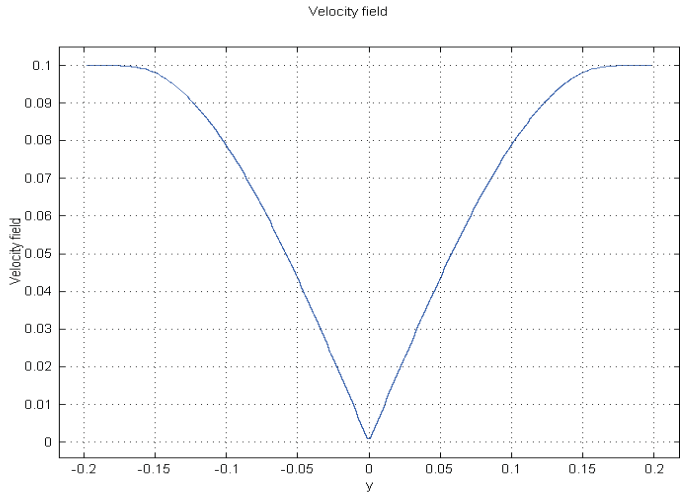

Figure 7.6: Velocity cross section, $x = 0$ - $l = 10^{0}$

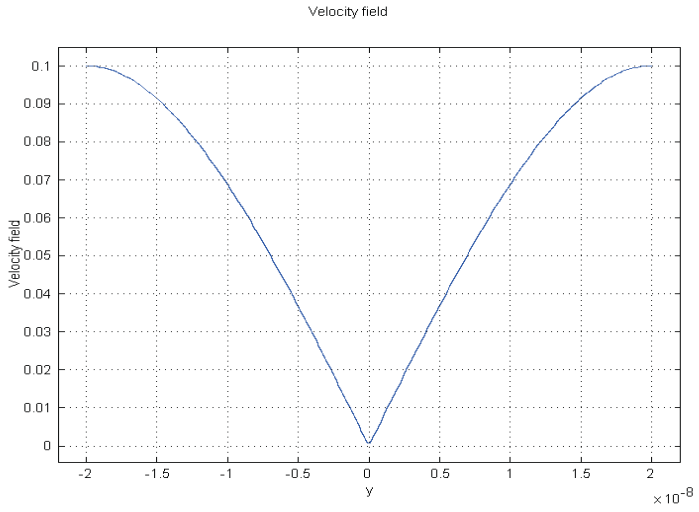

Figure 7.7: Velocity cross section, $x = 0$ - $l = 10^{-6}$

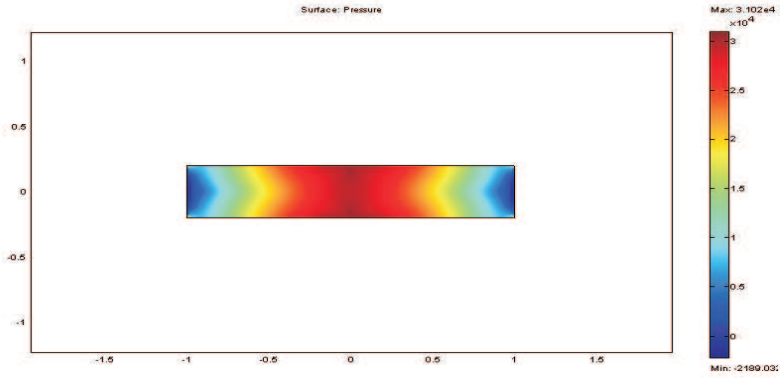

Figure 7.8: Pressure profile - $l = 10^0$

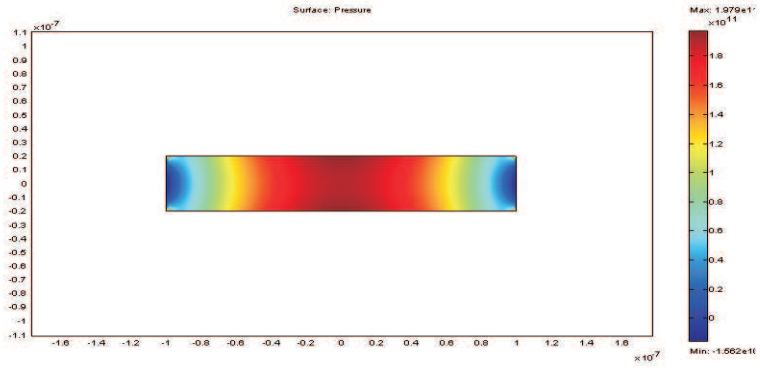

Figure 7.9: Pressure profile - $l = 10^{-6}$

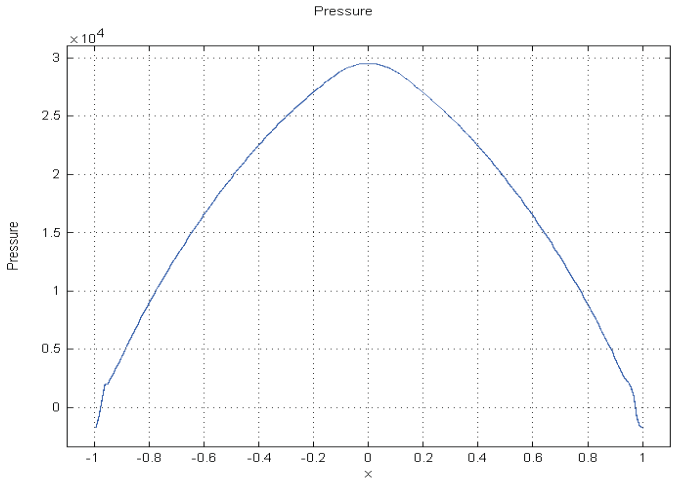

Figure 7.10: Pressure cross section $y = 0$ - $l = 10^{0}$

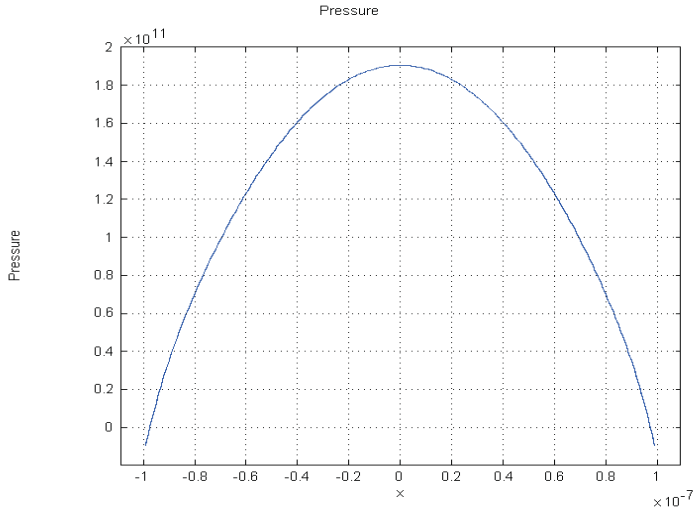

Figure 7.11: Pressure cross section $y = 0$ - $l = 10^{-6}$

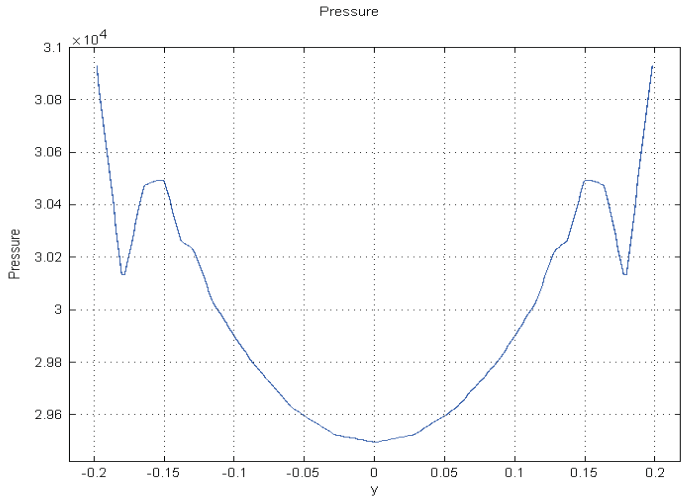

Figure 7.12: Pressure cross section $x = 0$ - $l = 10^{0}$

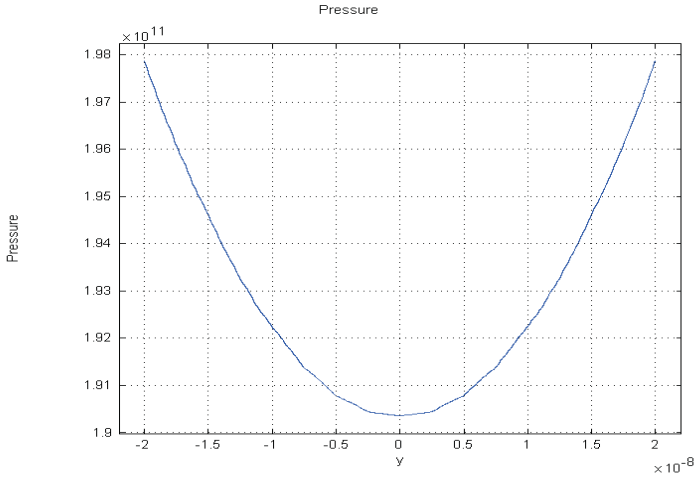

Figure 7.13: Pressure cross section $x = 0$ - $l = 10^{-6}$

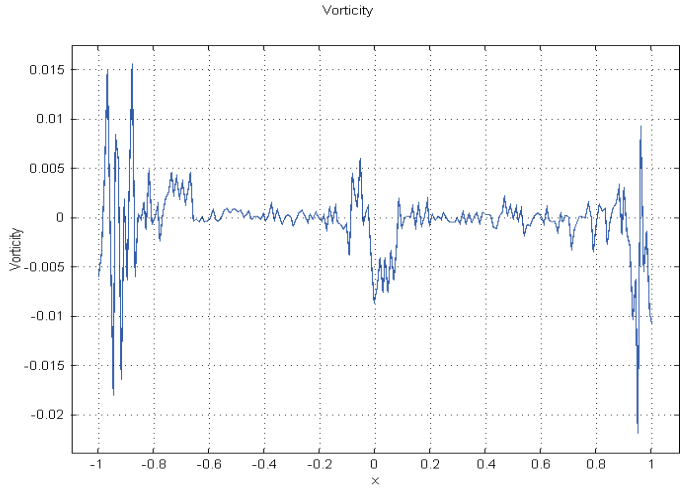

Figure 7.14: Vorticity cross section $y = 0$ - $l = 10^{0}$

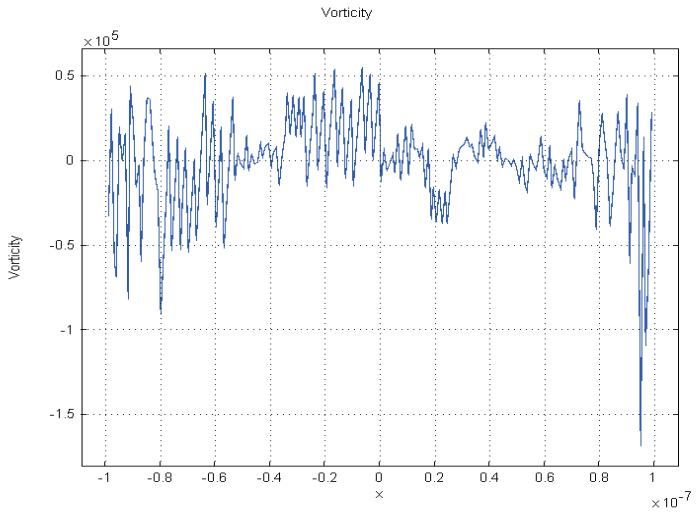

Figure 7.15: Vorticity cross section $y = 0$ - $l = 10^{-6}$

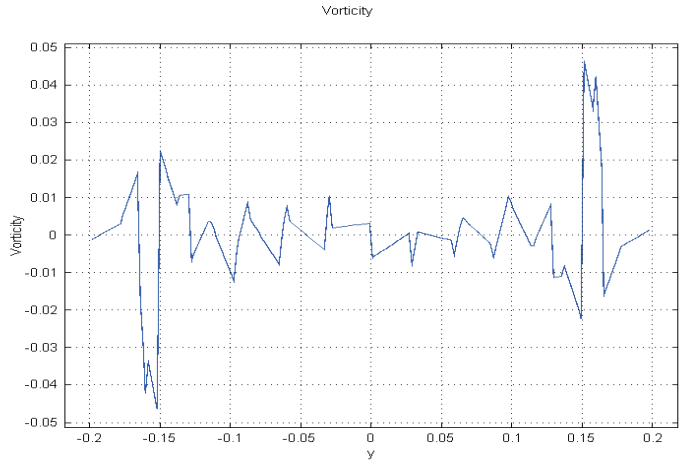

Figure 7.16: Vorticity cross section $x = 0$ - $l = 10^{0}$

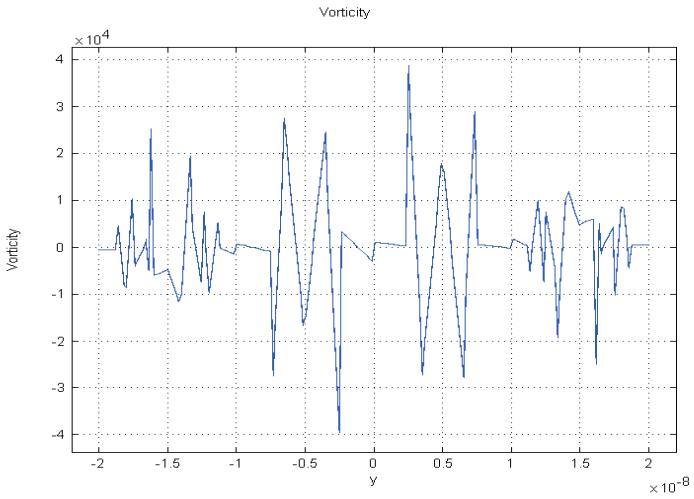

Figure 7.17: Vorticity cross section $x = 0$ - $l = 10^{-6}$

7.2.2 Disscussion of results

We begin by discussing the velocity profiles for our model. Figures 6.2 and 6.3 both show velocity profiles for the flow of our fluid, Figure 6.2 for the length scale $l = 10^0$ and Figure 6.3 for the length scale $l = 10^{-6}$. Both profiles have very similar appearences, and it is not easy to notice any differences between the two by these profiles alone. We take cross sections along the $x = 0$ and $y = 0$ sections. Concerning ourselves first with the $y = 0$ cross section, we see that there is very little to distinguish between our two length scales, Figures 6.4 and 6.5. The only difference noticable is at the top of the v-shape, the model for the $l = 10^0$ length scale flattens out earlier along the x-axis then for the other case. Looking at length scales between these two shows that the flattening out happens progressively latter as the length scale is decreased. The only other noticable difference is that the velocity increases at each respective point as the length scale is decreased, a common occurance amongst all three of our geometries that we have explored. If we now look at the cross section $x = 0$, we get a very similar situation as with the other cross section, the only major difference being that this cross section curves up more so towards the top of our v-shape, Figures 6.6 and 6.7. The curving of the v-shape occurs more in the model for the $l = 10^{-6}$ length scale than the $l = 10^0$ model. This means that the acceleration of the fluid particles at each point is less than the value of the acceleration at the same respective point in our $l = 10^0$ model.

Looking next at the pressure profiles, we see that in both cases our pressure is greatest in the middle of the fluid, along the $y = 0$ axis and decreases as we move away from this axis in both the positive and negative directions. This is what is to be expected as the fluid in the middle of our domain will experience more of the force of the plates coming together than fluid closer to the outflow boundaries. From these two presure profiles, it is also noticable that the pres-

sure in the $l = 10^{-6}$ model is at a greater pressure for a longer proportion of the length of the geometry than for the standard length case. The pressure also appears to distribute itself in a curved fashion for the smaller length, compared to the almost triangular fashion for the standard case - seen in regions where the pressure changes, we have curves for the $l = 10^{-6}$ case and triangles for the $l = 10^{0}$ case. The cross section across $y = 0$ shows similar distrubutions of the velocity, the $l = 10^{-6}$ case having a smoother and more gentler curve, resembling an inverted x^2 curve, whereas the 10^{0} case resembles an x^2 curve compressed together from the sides. There is also a variation at the edges of the plot, with the curve ending to give way to two almost straight vertical lines. This is evident on length scales between our two extremes, slowly vanishing to give way to a complete smooth curve at $l = 10^{-4}$. The cross section along $x = 0$ is entirely different. With reference to Figures 6.12 and 6.13, we see a curve with two major dips in it and slight fluctuation for our standard length scale and a smooth curve for our micron length scale, this time resembling an x^2 curve. Previous experience suggests to investigate intermediate lengths and doing so shows us that again as the length scale is decreased the major dips and fluctuations receed and we get a smooth curve - again this is completely achieved at $l = 10^{-4}$.

Our final discussion for this geometry involves the vorticity. With reference to our cross section plots, Figures 6.14, 6.15, 6.16, 6.17, it can be seen that there appears to be no pattern at all to describe the vorticity - it appears completely random and chaotic. The same results are achieved for length scales between the two we are investigating - all plots appear completely random.

Chapter 8

Conclusions and further work

8.1 Conclusion

We discuss non-Newtonian flows and various models describing the consitutive equations and explore the finite element method and how it can be adapted for non-Newtonian, visco-elastic flows. The software package FEMLAB is employed to generate results for our problem of determining the flow patterns formed for our three geometries for a viscoelastic fluid of Oldroyd-B type. Initially the problems were solved for a standard length scale, $l = 10^0$. The flow for the reduced length scale was then investigated down to a length scale in the order of microns in order to determine whether flow patterns change upon the minaturisation of flow devices.

Three geometries were investigated, all involving two parellel plates: the first with the plates stationary, the second with the top plate moving with velocity v and the third with the two plates moving toward each other. We found that in

all three geometries that both the velocity and pressure increase as the length of the flow device is decreased for equivalent points in the flow domain.

With our first geometry we have, in addition to the velocity increase, an increase in the velocity followed by a decrease to a smaller velocity just as it leaves the outflow boundary. This was not evident on the standard length scale, but appears as the length is reduced.

For our second geometry we observe extra clogging in the bottom left hand corner of our flow domain as the length scale is reduced. There is also an increase in clogging in a central region of the flow domain and the added effect that the velocity around this clogging is decreased for smaller length scales. There is also a small pocket of fluid in the top left hand corner that has a smaller velocity than its surroundings. As the length scale is reduced, this pocket moves closer to the left hand boundary.

For our final geometry we have very few differences between the different length scales, apart from a few small velocity/pressure differences.

In all three geometries the vorticity appears random and chaotic across the horizontal but has a more structured appearance across the vertical for the first two models, changing as the length is reduced. For the third model the vorticity appears chaotic and random along the vertical.

In answering the questions posed in the introduction, we can say that as the length is reduced toward the micron level the models for the flow of our viscoelastic fluid remain very similar to the standard length scale models, with a few differences here and there, but nothing too drastically different - mainly just velocity differences in some places.

In the selection of which model to use for the construction of the flow device, our findings would suggest that our third geometry is the better. There is little difference between models for different length scales, whereas for the other two there are issues that may cause problems. For the first model, we have the flow increasing and then decreasing on the smaller length scale models, a scenario that doesn't occur on our standard length. Although this isn't a problem as such, it would be a better bet to use a geometry which has not got any differences like this, i.e. the third geometry. With regards to the second geometry we have the problem of clogging to deal with, and this will become more relevant in the situations where our volume of fluid available is small. The clogging, although greater for small lengths, is a problem arising from the flow device.

8.2 Further work

8.2.1 Different geometries

The investigation of different geometries would be carried out in order to determine whether we could find a better geometry to model a flow device on. These different geometries could include the Taylor-Couette geometry, where a fluid is contained in the gap beween two cylinders and the outer cylinder rotates, or in a geometry where we have contraction channels.

8.2.2 Further investigation into geometry 2

In order to reduce the effect of clogging, perhaps an inflow could be introduced into the set-up, so we would have a flow of fluid into the device with the top plate still moving.

8.2.3 Even smaller length scales

An investigation into what happens to the flow patterns when the length scale is reduced down to the order of the size of the particles of the fluid could be carried out.

Acknowledgements

I would like to acknowledge Professor Geoff Mitchell for his underlying knowledge of this subject area and Professor Mike Baines for his assistance in solving the problems, without which this project would have been significantly more difficult. I would like to thank EPSRC for their financial contribution enabling me to take this Masters course. I would like to thank my friends off the course, particularly Stewart (for our fantastic chats!), Phil, Shaun and Jon. I would like to thank my family for their help during the year, particularly my Grandparents who have helped with numerous issues. Last but not least I would like to thank Pip for being there throughout the year with continuous support and love and probably the most important thing - giving me the necessary few hard words when I wasn't working or was leaving work to the last minute!

Bibliography

[1] Bird, Armstrong, Hassager: *John Wiley & Sons* Dynamics of Polymeric Liquids Volume 1 Fluid Mechanics, Second Edition (1987)

[2] Nikita Ter-Oganessian: *Technische Universität München* Active microrheology of semiflexible polymer solutions: computer simulations and scaling theory, (23-08-2004)

[3] Dirac *Oxford University Press* The Principle of Quantum Mechanics, Third edition (1947)

[4] F. Brezzi & M. Fortin: *Springer-Verlag* Mixed and Hybrid finite element method (1991)

[5] David Currie: *University of Cardiff* Stable Finite Element approximations for viscoelastic flow problems, Dissertation for MSc (Sept 2004)

[6] E.Suli & D. Mayers: *Cambridge University Press* An introduction to Numerical Analysis (2003)

[7] $http://en.wikipedia.org/wiki/Finite_element_method$

[8] Crochet, Davies, Walters: *Elsevier* Numerical Simulation of Non-Newtonian Flow (1984)

[9] V.Legat & J.M.Marchal: *Journal of Rheology* On the stability and accuracy of fully coupled finite element techniques used to simulate the flow of differential viscoelastic fluids: a one-dimensional problem (1992)

[10] http://www.csc.fi/cschelp/sovellukset/math/matlab/femlab/femlab/femlabTOC.htm

[11] M.A.Wakefield, edited by J.M.Melenk *lecture notes, University of Reading* Iterative Solution of Large Linear Systems, Spring 2005

[12] O Axelsson *Cambridge University Press* Iterative Solution Methods, (1993)